JOURNAL OF GEOPHYSICAL RESEARCH, VOL. 112, A01303, doi:10.1029/2006JA011982, 2007

Observations of ionospheric convection from the Wallops SuperDARN radar at middle latitudes

J. B. H. Baker,[1] R. A. Greenwald,[1] J. M. Ruohoniemi,[1] K. Oksavik,[1] J. W. Gjerloev,[1] L. J. Paxton,[1] and M. R. Hairston[2]

Received 19 July 2006; revised 16 October 2006; accepted 9 November 2006; published 20 January 2007.

[1] During geomagnetic storms the ability of the Super Dual Auroral Radar Network (SuperDARN) to measure ionospheric convection becomes limited when the radars suffer from absorption and the auroral disturbance expands equatorward of the radar sites. To overcome these shortcomings, it was decided to construct a SuperDARN radar at middle latitudes on the grounds of the NASA Wallops Flight Facility. This paper presents the first comprehensive analysis of Doppler measurements from the Wallops radar, which commenced operations in May 2005. Wallops measurements are compared with the Goose Bay radar during the onset of a geomagnetic storm on 31 August 2005: Goose Bay measured the onset of geomagnetic activity at high latitude while Wallops monitored the expansion of convection to middle latitudes. Average convection patterns binned by the *Kp* geomagnetic index are also presented. During weak-moderate geomagnetic activity ($Kp \leq 3$) the Wallops radar observes ionospheric irregularities between 50° and 60° magnetic latitude drifting westward across much of the nightside. When these measurements are incorporated into the calculation of an average SuperDARN convection pattern, the streamlines of polar cap outflow on the nightside become kinked in a manner reminiscent of the Harang discontinuity. This morphology arises quite naturally when the two-cell convection at high latitudes merges with the prevailing westward convection at middle latitudes. During increased geomagnetic activity ($Kp \geq 3$), Wallops is able to measure the expansion of auroral electric fields to middle latitudes and the average SuperDARN cross-polar cap potential is increased by 25%.

Citation: Baker, J. B. H., R. A. Greenwald, J. M. Ruohoniemi, K. Oksavik, J. W. Gjerloev, L. J. Paxton, and M. R. Hairston (2007), Observations of ionospheric convection from the Wallops SuperDARN radar at middle latitudes, *J. Geophys. Res.*, *112*, A01303, doi:10.1029/2006JA011982.

1. Introduction

[2] Plasma convection in the Earth's ionosphere at high latitudes is tightly coupled to the circulation of plasma in the outer regions of the magnetosphere via magnetic field lines. The primary energy source driving magnetospheric circulation is a dawn-dusk electric field across the magnetotail produced by interactions with the solar wind at the magnetopause, most notably, during periods of southward directed interplanetary magnetic field (IMF). Usually, the ionospheric convection conforms to a well-known two-cell pattern characterized by antisunward convection over the highest latitudes of the polar cap and sunward return flow along the dawn and dusk flanks at auroral latitudes. It is in this latter region, the auroral zone, that the processes of magnetosphere-ionosphere coupling are most prominently manifested through intense electric fields, large electric currents, and dramatic displays of visible aurora. Under normal conditions, the auroral zone is generally believed to have a sharp equatorward boundary at approximately 60° invariant magnetic latitude on the nightside [*Holzworth and Meng*, 1975; *Heppner and Maynard*, 1987]. Equatorward of this boundary the midlatitude ionosphere is coupled to the plasmasphere and radiation belts of the inner magnetosphere. It is generally assumed that these regions are, to some extent, "shielded" from the effects of the cross-tail convection electric field by a counter-acting polarization electric field that develops at the inner edge of the plasma sheet. As a consequence, the midlatitude ionosphere is generally free of the strong electric fields, field-aligned currents, and energetic particle precipitation that are characteristic of higher latitudes.

[3] A number of studies have investigated how ionospheric convection at high latitudes depends on the orientation of the IMF. The earliest papers [*Heppner*, 1977; *Heppner and Maynard*, 1987] presented qualitative patterns of ionospheric convection that were ordered by IMF clock angle. Later studies used more quantitative techniques to characterize the convection in terms of IMF orientation and season using a variety of data sets: Defense Meteorological

[1] Applied Physics Laboratory, Johns Hopkins University, Laurel, Maryland, USA.
[2] W. B. Hanson Center for Space Sciences, University of Texas at Dallas, Richardson, Texas, USA.

0148-0227/07/2006JA011982$09.00

Satellite Program (DMSP) [*Rich and Hairston*, 1994]; Dynamics Explorer spacecraft [*Weimer*, 1995]; inversion of ground-based magnetometer measurements [*Friis-Christensen et al.*, 1985; *Papitashvili et al.*, 1994]; the HF radars of the Super Dual Auroral Radar Network (SuperDARN) [*Ruohoniemi and Greenwald*, 1996, 2005]; and incoherent scatter radar [*Foster*, 1987; *Holt et al.*, 1987]. Although there is some disagreement about the overall strength of convection in these models as characterized by the cross-polar potential (Φ), the general morphologies of the convection patterns are largely consistent with each other. During southward IMF (negative *Bz*) the convection pattern has a well-defined two-cell structure and Φ tends to increase with the magnitude of southward *Bz*. During northward IMF the convection weakens and the pattern can break apart, with one or more additional cells of reversed convection appearing in the polar cap on the dayside (so-called ''lobe cells''). The statistical models also display second-order IMF *By* dependencies such that during periods of positive (negative) IMF *By* the dusk (dawn) cell becomes more dominant and rounded. These morphological features are consistent with reconnection being the dominant process in solar wind–magnetosphere interactions [*Dungey*, 1961; *Crooker*, 1979; *Reiff and Burch*, 1985].

[4] Some of the disagreement about the size of Φ between the various empirical models of high-latitude ionospheric convection can perhaps be attributed to the different data sets and statistical techniques used. It is fair to say that the models based on SuperDARN data [*Ruohoniemi and Greenwald*, 1996, 2005] tend to have weaker cross-polar potentials compared with the others. One possible reason for this distinction may be a limit on the range of geomagnetic activity levels for which the SuperDARN radars have hitherto been effective at measuring the full spatial extent of the high-latitude convection. During extreme geomagnetic disturbances it is known that SuperDARN radars suffer a reduction in data capture for two reasons: (1) The auroral zone expands equatorward and out of the radar field of view, and (2) enhanced precipitation in the polar cap and auroral zone leads to heavy absorption of radar signals in the ionospheric *D* layer. To overcome these shortcomings, it was decided to build an HF radar at the NASA Wallops Flight Facility in Virginia (invariant latitude 49.4°N), approximately 10°–15° equatorward of the existing array of Northern Hemisphere radars at 60°–65° invariant latitude. The primary motivation for building the Wallops radar at this latitude was to improve the capability of the SuperDARN network for monitoring convection during periods of enhanced geomagnetic activity. The design of the Wallops radar also includes a number of innovations that improve performance and reduce the cost of installing the system; these innovations will be explained in section 2.2. Construction of the Wallops radar began in December 2004, and the radar became fully operational in May 2005.

[5] Another motivation for building a SuperDARN radar at middle latitudes was to investigate the physics of mid-latitude electric fields. In recent years there has been substantial interest in understanding the mechanisms that produce electric fields at middle latitudes and the role they play in structuring ionospheric plasma [e.g., *Basu*, 2001]. This type of analysis has already been an early focus of study with the Wallops radar. *Greenwald et al.* [2006] compared Wallops radar observations with measurements from the Millstone Hill incoherent scatter radar and found that the temperature gradient instability at the plasmapause boundary was the most likely mechanism for creating a particular category of the subauroral irregularities observed by the Wallops radar. A number of studies have used measurements from satellite-based ion drift meters [*Heelis and Coley*, 1992] or incoherent scatter radar [e.g., *Blanc and Amayenc*, 1979; *Wand and Evans*, 1981; *Buonsanto et al.*, 1993; *Buonsanto and Witasse*, 1999] to categorize the average pattern of midlatitude ion drifts under quiet and disturbed conditions, and as functions of season and solar cycle. However, to some extent these studies have produced contradictory pictures of how midlatitude convection is ordered by season and solar cycle. Much of the inconsistency may have to do with the fact that ion drifts at middle latitudes tend to be weak and highly variable, making it hard to characterize typical behavior. The Wallops radar provides new opportunities to examine midlatitude electric fields with unprecedented spatial coverage and temporal resolution.

[6] Previous studies have identified four categories of midlatitude electric field that might be observed by the Wallops radar. The first electric field appears at middle latitudes when the high-latitude convection system and its associated shielding layer both move equatorward during geomagnetic storms. We refer to this as an ''auroral electric field'' in recognition of its direct connection to auroral processes occurring at higher latitudes. The second category of midlatitude electric field appears equatorward of the auroral oval but poleward of the shielding layer during disturbed periods and drives flows that are noticeably detached from the high-latitude convection system [*Galperin et al.*, 1974; *Spiro et al.*, 1978; *Anderson et al.*, 1991; *Yeh et al.*, 1991; *Foster and Rich*, 1998; *Anderson et al.*, 2001; *Foster and Vo*, 2002]. These flows were recently categorized as subauroral polarization streams (or SAPS), and it is postulated that they are driven by polarization electric fields that arise when field-aligned currents are imposed across the low conductance region of the midlatitude ionospheric trough [*Foster and Burke*, 2002]. We call this second category a ''SAPS electric field.'' The third electric field is observed when there is a breakdown in the compensatory system of currents and electric fields that normally shields the midlatitude ionosphere from the effects of the convection electric field; the classic example is a large and sudden southward turning of the interplanetary magnetic field. This category is called a ''penetration electric field'' because it is of magnetospheric origin but observed equatorward of the shielding layer [e.g., *Huang et al.*, 2006]. The fourth category is driven by ion-neutral interactions. Observations from incoherent scatter radars often see a latitudinally extended region (10°–20°) of low-velocity westward drift in the nightside subauroral ionosphere [*Blanc et al.*, 1977; *Huang et al.*, 2001]. Modeling by *Blanc and Richmond* [1980] has suggested that these drifts are produced by the dynamo action of zonal winds. During quiet times the winds are driven by diurnal and semidiurnal tides; during disturbed periods they can become enhanced by auroral heating and increased ion-neutral collisions. The plasma drift exiting the polar cap on the nightside acquires an east-west component from the

Coriolis force. We refer to this category as a "neutral dynamo electric field."

[7] The primary goal of this paper is to present the first comprehensive analysis of Doppler velocities from the Wallops radar and demonstrate the impact that midlatitude measurements have on the calculation of SuperDARN convection patterns, particularly during periods of heightened geomagnetic activity. The structure of the rest of the paper is as follows. Section 2 presents a brief description of the SuperDARN radars and some of the analysis techniques used, with a particular emphasis on describing the innovations in the Wallops radar design. Section 3 presents the results in two main parts: an event analysis in which Wallops data are examined during the onset of a geomagnetic storm on 31 August 2005 and compared with other measurements (section 3.1); and the presentation of statistical patterns of ionospheric convection binned by the *Kp* geomagnetic index (section 3.2). This is followed by a discussion section, which reviews the Wallops results and places them in the context of previous studies of midlatitude ionospheric convection (section 4). The final section of the paper (section 5) is a brief summary and conclusions.

2. Data Sets and Techniques

[8] In this section we provide a brief review of the SuperDARN radars (section 2.1) and describe some of the unique capabilities of the Wallops radar (section 2.2). The methodology used for integrating line-of-sight velocity data from the entire SuperDARN network for the purpose of calculating ionospheric convection patterns is briefly described in section 2.3.

2.1. Super Dual Auroral Radar Network (SuperDARN)

[9] SuperDARN is a network of high-frequency (HF) radars for ionospheric research that was developed with funding from 12 countries. SuperDARN radars are sensitive to scatter from decameter-scale irregularities in the ionospheric plasma density, which have been amplified above thermal fluctuation levels by plasma instabilities [*Fejer and Kelley*, 1980]. The irregularities are highly field aligned and therefore present an appreciable cross section for backscattering only when the HF ray is directed within a few degrees of perpendicularity to the magnetic field. This orthogonality condition for the radar signal is achieved via refraction in the ionosphere. At *F* region heights, the Doppler shift of the backscattered signal measured by the radar is directly related to the plasma convection velocity and the ionospheric electric field [*Villain et al.*, 1984; *Ruohoniemi et al.*, 1987]. It should be pointed out that the ability of SuperDARN radars to measure plasma drift velocities at a particular time and location is dependent on the presence of the plasma irregularities to provide backscatter targets for the radar signal. Other factors that affect the data capture rate at a particular location are (1) auroral absorption of the signal along the propagation path; (2) propagation conditions that prevent the radar signal from reaching that location; (3) clutter from signals reflected off the ground (i.e., groundscatter); and (4) interference from other sources of HF signal.

[10] The design of the SuperDARN radars has evolved significantly from that of the original Goose Bay radar, which became operational in 1983 [*Greenwald et al.*, 1985]. A detailed description of SuperDARN as it existed at the start of the International Solar Terrestrial Physics (ISTP) mission is given by *Greenwald et al.* [1995]. In brief, the standard SuperDARN radar utilizes an array of electronically phased antennas that can be steered in 16 distinct beam directions within a field of view spanning an azimuth sector of 52°. A special multipulse sounding sequence is used to unambiguously determine the range and Doppler velocity of the ionospheric irregularities out to ranges in excess of 3000 km. A secondary antenna array provides vertical angle-of-arrival information that can be used to determine the altitude of the irregularities. All SuperDARN radars operate continuously using a variety of sounding modes. In standard operation the temporal resolution is 1–2 min and the range resolution is 15–45 km. While there are some hardware differences between the various radars, each is controlled with a common set of software and produces identical data products. This approach enables straightforward analysis of data obtained from the entire SuperDARN network.

2.2. Wallops Radar

[11] As mentioned in the introduction, the SuperDARN radars have been most effective at measuring ionospheric convection during periods of weak to moderate geomagnetic activity. This restriction is partially associated with the fact that the radars cannot view the convection equatorward of the radar locations, at approximately 60° invariant latitude. To overcome this shortcoming and extend the latitudinal coverage of SuperDARN to middle latitudes, it was decided to build a new HF radar at the NASA Wallops Flight Facility (WFF) in Virginia (37.9°N, 75.5°E geographic; 49.4°N and 0.1°E Altitude Adjusted Corrected Geomagnetic (AACGM) magnetic). The Wallops radar was constructed as a joint project with funds provided by the WFF and the Johns Hopkins University Applied Physics Laboratory. Construction began at WFF in December 2004, and the radar commenced operations in May 2005. The hardware design for the Wallops radar includes two notable innovations. First, it uses a new type of phasing matrix that allows more flexibility in selecting viewing directions for the transmitted and received signals. This new phasing matrix allows the radar to steer in directions outside the nominal field of view but with a corresponding reduction in sensitivity. The second innovation is that the Wallops radar utilizes a twin-terminated folded dipole antenna with an integral corner reflector, rather than the log-periodic antennas that are used on most of the other SuperDARN radars. The new antenna greatly reduces the hardware installation cost and improves the front-to-back ratio at lower frequencies.

[12] The Wallops radar employs the same modes and control software as the other SuperDARN radars but transmits a longer pulse sequence, which extends the range of the radar from 75 range gates (3375 km) to 110 range gates (4950 km). The decision to extend the range of the Wallops radar was made when early operations demonstrated that the radar can detect backscattered signals from the ocean surface out to these ranges. However, under most condi-

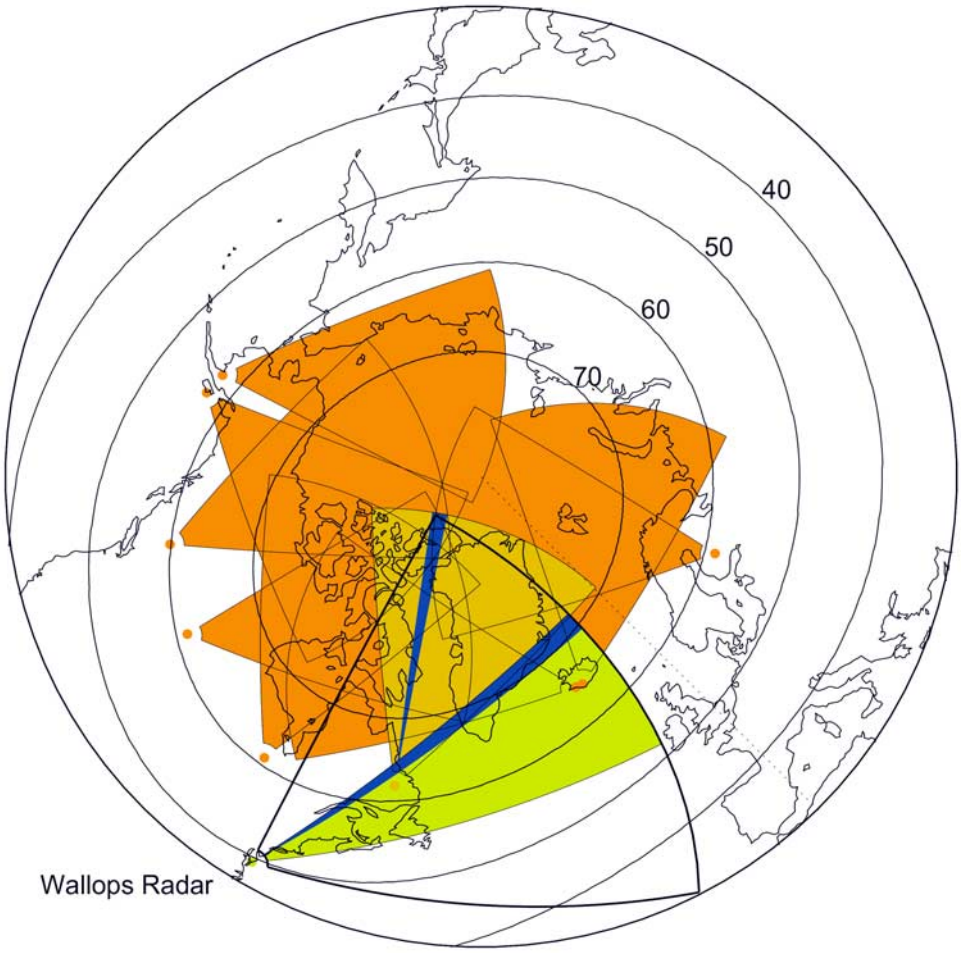

Figure 1. The combined field of view (FOV) of the 10 Northern Hemisphere SuperDARN radars in operation between May 2005 and April 2006. High-latitude radars are shaded orange, except Goose Bay, which is shaded yellow. The full FOV for the Wallops radar is bounded by heavy lines; the central green-shaded region identifies the Wallops FOV between May and December 2005. The Goose Bay and Wallops beams on which measurements are compared in sections 3.1.2 and 3.1.3 are colored blue.

tions, significant ionospheric backscatter is only observed out to ranges of 3000 km. Figure 1 shows the combined fields of view (FOV) of the 10 Northern Hemisphere SuperDARN radars in operation between May and September 2005. The FOVs for the majority of the high-latitude radars are shaded orange. For emphasis, Goose Bay's FOV is shaded a pale yellow color; section 3.1 includes a beam-to-beam comparison between Wallops and Goose Bay measurements (these two beams are colored blue). The full FOV for the Wallops radar is bounded by heavy lines and divided into three segments: two unshaded segments flanking a central green-shaded segment. The green-shaded region identifies the FOV that applied between May and December 2005. Starting in January 2006, after the steering performance of the antenna array was better understood, the azimuthal coverage of the Wallops radar was increased to include both the shaded and unshaded segments. This configuration obtains measurements in 24 beam directions with a separation of 3.24° and covering a combined azimuth sector of 78°. Note also that the increased range of the Wallops radar compared to the higher-latitude radars is also apparent in Figure 1.

2.3. SuperDARN Ionospheric Convection Patterns

[13] The primary objective of SuperDARN is to provide direct, continuous, global-scale observations of high-latitude ionospheric convection. An analysis procedure first developed by *Ruohoniemi and Baker* [1998], and further developed by *Shepherd and Ruohoniemi* [2000], combines all available SuperDARN Doppler data within a hemisphere to compile an ionospheric convection pattern. This procedure consists of a number of steps, which are now briefly described. In the first step all of the Doppler velocity data are median filtered in range, azimuth, and time to remove noise and marginal values. The filtered data are then binned onto a uniform spatial grid of equal area cells. The spatial binning is necessary to prevent over-sampling of the near-radar regions relative to the far-radar regions in the final solution. The second step is to select an equatorward boundary for the convection zone where the electrostatic potential will be set to zero. It is assumed that this boundary conforms to the average shape determined by *Heppner and Maynard* [1987] but it can expand equatorward or contract poleward uniformly at all local times while maintaining its shape. We thus specify a particular Heppner-Maynard (HM)

boundary uniquely by identifying the latitude at which it crosses magnetic midnight. In practice, the HM boundary is determined by examining the gridded line-of-sight velocity magnitudes as a function of magnetic latitude and magnetic local time [*Shepherd and Ruohoniemi*, 2000]. In each local time sector we look for a steep decline in velocity magnitude at some particular latitude; least squares fitting is then used to identify the particular HM boundary that provides the closest fit through these points. As a practical consideration, the radars are most effective at identifying the HM boundary when they are located on the dayside and the bulk of the convection is poleward of the radar sites. The third step is to estimate the ionospheric velocities in regions of poor data coverage using a "background pattern"; this is necessary to prevent the fitted solution from becoming unphysical in these regions. Time-shifted measurements of the IMF from interplanetary spacecraft are generally used to select an appropriate background pattern from statistical patterns of ionospheric convection binned by IMF configuration [*Ruohomiemi and Greenwald*, 1996]. These statistical patterns are ordered by the magnitude of the IMF vector in the *Bz-By* plane (B_T) and the corresponding clock angle sector. Last, the fourth step is to solve Laplace's equation to obtain a solution for the ionospheric electrostatic potential as a weighted least squares fit to a spherical harmonic expansion of associated Legendre functions. The velocity estimates from the IMF statistical model are weighted lower than the gridded line-of-sight data to ensure that the IMF model constrains the solution in regions of poor data coverage but does not unduly influence the results in the vicinity of the velocity measurements. Differences between the input convection velocity measurements and the fitted velocity values can be used to evaluate the quality of the potential solution. In recent years, SuperDARN convection patterns derived from this procedure have become an invaluable tool for space weather now casting. SuperDARN convection patterns have also been used to investigate a number of topics in magnetosphere-ionosphere coupling, such as the response of ionospheric convection to influences in the interplanetary medium [e.g., *Ruohoniemi and Greenwald*, 1998; *Milan et al.*, 2000; *Nishitani et al.*, 2002; *Chisham et al.*, 2004; *Watanabe et al.*, 2004].

3. Results

[14] The results section can be divided into two parts: an event analysis covering the first few hours of a geomagnetic storm (section 3.1) and a statistical analysis of average ionospheric convection patterns binned by the *Kp* magnetic index.

3.1. Event Study: 0900–2400 UT on 31 August 2005

[15] In this section we present a detailed description of the onset of a geomagnetic storm on 31 August 2005. Measurements from the Wallops radar (section 3.1.3) are compared with simultaneous observations obtained at higher latitudes by the Goose Bay radar in the same longitude sector (section 3.1.2). The motivation is to demonstrate some of the unique capabilities of Wallops compared with the other SuperDARN radars. The effect that Wallops data have on the calculation of SuperDARN convection patterns during this event is also examined (section 3.1.4). In section 3.1.5 a more comprehensive picture of the event is presented by including DMSP (Defense Meteorological Satellite Program) drift meter measurements in the calculation of convection patterns and relating the convection features to auroral images obtained from the Thermosphere-Ionosphere-Mesosphere Energetics and Dynamics (TIMED) spacecraft Global Ultraviolet Imager (GUVI) instrument. We first provide a wider geophysical context for the event interval by describing the prevailing interplanetary conditions and the behavior of magnetic indices on 31 August 2005 (section 3.1.1).

3.1.1. Magnetic Indices and Interplanetary Conditions

[16] Magnetic indices provide a simple means of characterizing the overall level of geomagnetic activity as a function of universal time. The *SYM-H* and *Kp* indices characterize the strength of the ring current and the overall level of geomagnetic activity, respectively. Level 2 data obtained from the Solar Wind Electron, Proton, and Alpha Monitor (SWEPAM) [*McComas et al.*, 1998] and magnetometer (MAG) [*Smith et al.*, 1998] instruments aboard the Advanced Composition Explorer (ACE) spacecraft provide information about interplanetary conditions. Figure 2 shows time series of interplanetary and magnetospheric parameters on 31 August 2005. The parameters from top to bottom are IMF *By* (Figure 2a), IMF *Bz* (Figure 2b), solar wind density (Figure 2c), solar wind bulk velocity (Figure 2d), *SYM-H* magnetic index (Figure 2e), and *Kp* magnetic index (Figure 2f). On the basis of the location of the ACE spacecraft at (225, 16, −12) R_E on this particular day and an average prevailing solar wind speed of 402 km/s we calculate a transit time of approximately 57 min from the ACE spacecraft to the dayside magnetopause. The SWE and MAG measurements shown in Figure 2 (top four panels) have been time-shifted by this average propagation time.

[17] The time histories of the parameters shown in Figure 2 are consistent with the onset of a geomagnetic storm in the middle of the day. Starting at 1213 UT, from an initial value of 35 nT, the *SYM-H* index steadily decreased over a period of 7 hours and registered a minimum value of −119 nT at 1909 UT. During this same period the *Kp* index steadily increased in magnitude, reaching a maximum 3-hour value of *Kp* = 7 between 1500 and 1800 UT. The behavior of both magnetic indices is consistent with a steady buildup in the strength of the ring current between 1200 and 1900 UT. The peak of the storm can be estimated at approximately 1900 UT when *SYM-H* was most negative; recovery occurred on the following day at approximately 0700 UT when *SYM-H* had returned to values greater than −50 nT.

[18] The time-shifted ACE measurements (top four panels) provide information about the interplanetary driving influences for the storm. The solar wind bulk velocity underwent a number of small stepwise increases during the day and varied in the range 330–480 km/s. The solar wind proton density is missing prior to 0900 UT in the level 2 SWE data set, but between 0900 and 1300 UT it increased relatively smoothly from 12 to 46 particles per square centimeter and then declined haphazardly for the rest of the day. Of particular importance is the fact that the IMF *Bz* component at the dayside magnetopause turned southward at approximately 1157 UT and remained large and negative most of the time during the second half of the day. We therefore speculate that the increased geomagnetic activity

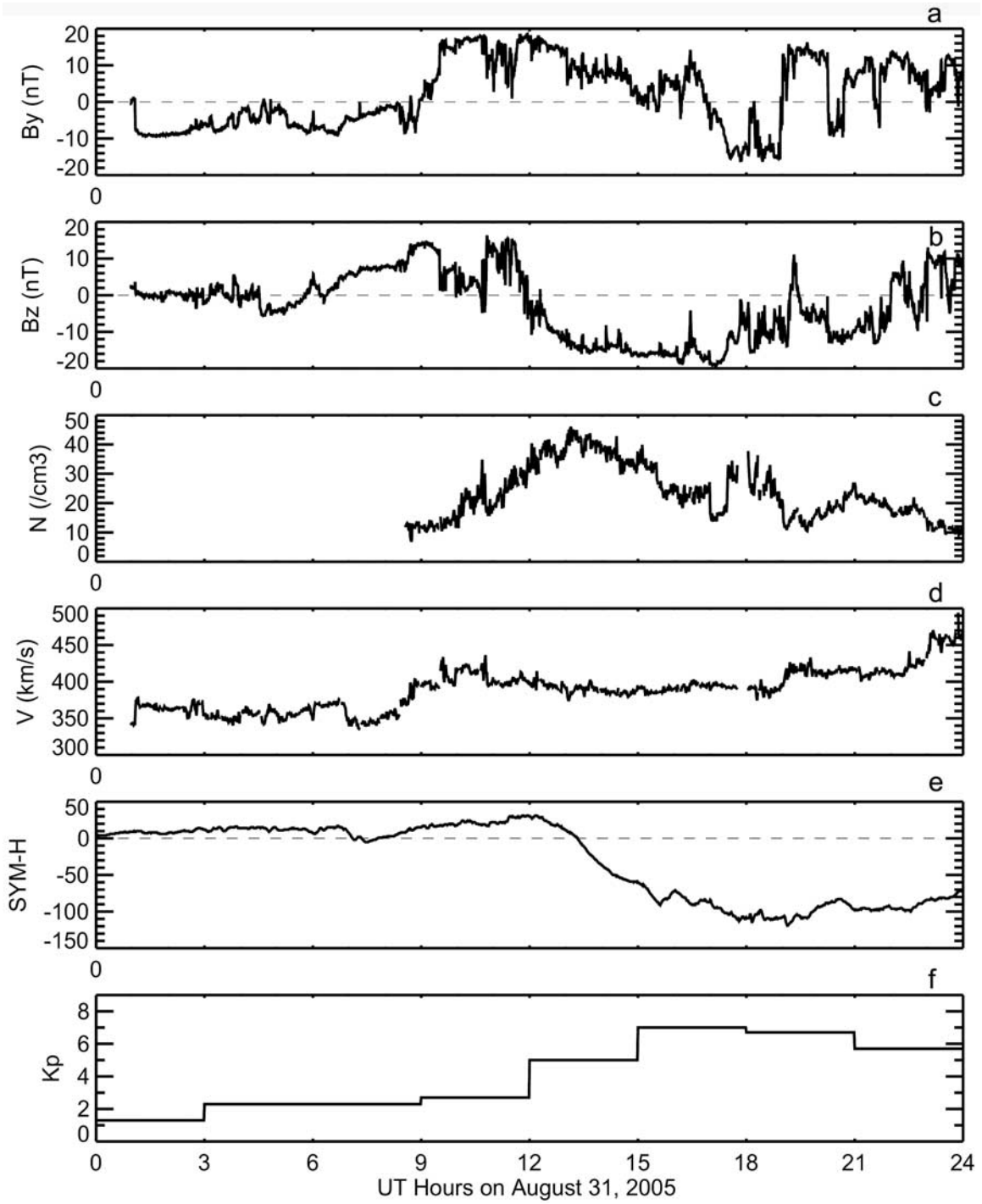

Figure 2. Time series of interplanetary and magnetospheric parameters on 31 August 2005. The parameters are (a) IMF *By*, (b) IMF *Bz*, (c) solar wind density, (d) solar wind bulk velocity, (e) *SYM-H* magnetic index, and (f) *Kp* magnetic index. The top four parameters were obtained from the ACE spacecraft and have been time-shifted 57 min to account for propagation to the dayside magnetopause.

measured in the *SYM-H* and *Kp* indices starting at approximately 1200 UT was most likely produced by a southward turning of the IMF *Bz* and an enhancement in the solar wind density.

3.1.2. Goose Bay Radar Measurements

[19] Figure 3 shows time series plots of measurements from the Goose Bay radar obtained between 0900 and 2400 UT on 31 August 2005. The data were collected on beam 4, which is closely aligned with the magnetic meridian (see Figure 1). The parameters from top to bottom are backscattered power (Figure 3a), line-of-sight velocity (Figure 3b), and spectral width (Figure 3c). The horizontal axes represent universal time while the vertical axes represent AACGM latitude. Each parameter is color-coded according to the color bars displayed on the right. In the middle panel, blue coloring indicates velocities toward the

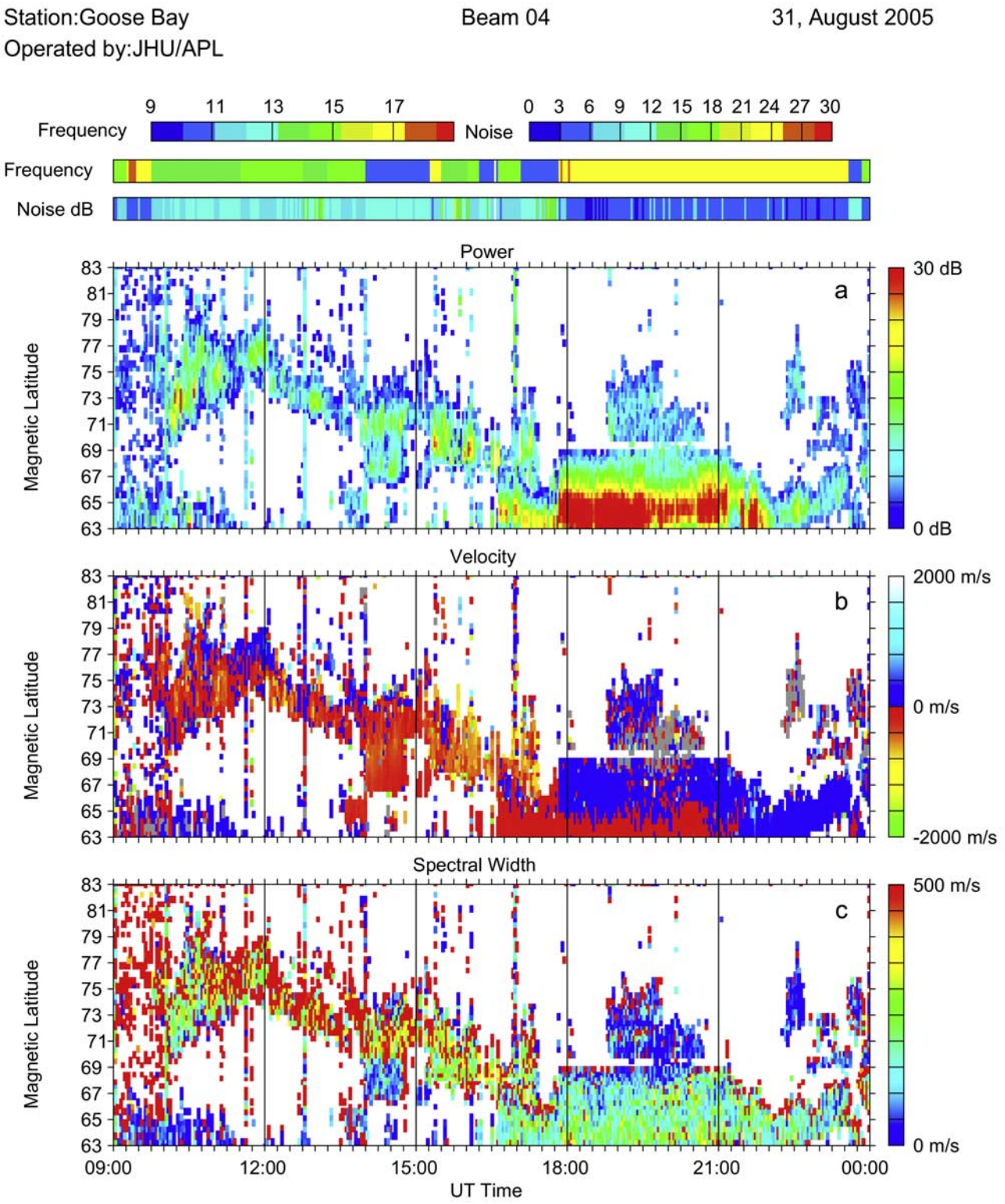

Figure 3. Parameter plot for beam 4 of the Goose Bay radar between 0900 and 2400 UT on 31 August 2005. Horizontal axis is universal time; vertical axis is magnetic latitude. Parameters shown are (a) backscattered power, (b) line-of-sight velocity, and (c) spectral width. Each parameter is color-coded according to the color scales on the right. Blue (red-green) coloring in Figure 3b indicates velocities toward (away from) the radar. Grey shading in Figure 3b identifies measurements flagged as groundscatter. Color-coded time series of the transmitted frequency and the measured noise are provided at the top.

radar while red-green colors correspond to velocities away from the radar. Areas of grey shading identify velocity measurements that have been flagged as groundscatter based on simultaneously low values of spectral width and velocity magnitude. At the top of the figure are color-coded time series of the transmitted frequency and the receiver noise. On this particular day the Goose Bay and Wallops radars were both operating in a ''sounding mode,'' which uses the available dead time in the scan cycle to sound the ionosphere on alternative frequencies. The radar uses the time history of sounding statistics to decide whether it should change to a new operating frequency that will increase the amount of ionospheric scatter. A disadvantage of the sounding mode is that it can confuse the interpretation of the radar time series. In particular, it can become difficult to distinguish targets that evolve in range and time according to varying geophysical conditions from those that simply appear and disappear in response to altered propagation paths associated with the frequency changes.

[20] We now interpret the Goose Bay radar measurements in the context of the overall level of geophysical activity suggested by the magnetic indices and compare the Goose Bay measurements with data gathered from the other SuperDARN radars. At 0900 UT the Goose Bay radar was not seeing very much scatter; what it did see tended to be distributed in range and rather noisy in appearance, possibly owing to interference from other HF sources. The scatter in the nearest range gates is most likely associated with *E* region echoes and/or scatter from meteor trails; as such, these measurements can be effectively ignored in a discussion of *F* region plasma convection. Starting at 0958 UT, Goose Bay began to see ionospheric scatter form in a well-defined region centered at approximately 72° invariant latitude. The Doppler velocities in this region were predominantly away from the radar, which for this particular beam corresponds to a magnetic north direction; the measurements are thus consistent with the radar observing the sunward flow along the flank of the dawnside convection cell. Over the next 2 hours (1000–1200 UT) this region of backscatter became better defined in range and started to retreat poleward. The occasional appearance of velocities directed toward the radar at the farthest ranges implies that the radar was measuring velocities in the vicinity of the dawnside convection reversal boundary. We interpret the poleward retreat of the backscatter between 1000 and 1200 UT as being predominantly associated with a diurnal variation (i.e., the local-time dependence of the magnetic latitude of the auroral zone), rather than with a change in geophysical conditions; in other words, it is not a poleward contraction of the polar cap. Examination of the data from the other SuperDARN radars between 1000 and 1200 UT confirms that the lower-latitude extent of the Doppler measurements remained largely static during this period.

[21] At 1200 UT the backscatter measured by Goose Bay had retreated to its most poleward point and was starting to move equatorward again. In this particular case, the bulk motion of the scatter is due predominantly to changing geophysical conditions (i.e., an expansion of the polar cap), but it also includes a smaller diurnal component associated with the fact that the radar was moving across the convection throat region toward the dusk cell. This is corroborated by the *SYM-H* (see Figure 2) and quick-look *AE* indices (not shown), which both show the onset of steadily increasing geomagnetic activity at this time; it is also consistent with the estimated arrival time for a southward IMF at the magnetopause at approximately 1157 UT (see Figure 2). We therefore speculate that the equatorward motion of the scatter that started at approximately 1200 UT is due predominantly to magnetic reconnection occurring at the magnetopause and an expanding polar cap. This will become clearer when we present the time series of convection patterns in section 3.1.4. Figure 3 shows that the equatorward expansion of the polar cap progressed on a timescale of several hours. From 1200 to 1640 UT the overall trend in the Goose Bay measurements is for the backscatter to steadily move equatorward to lower latitudes.

[22] At 1640 UT the Goose Bay radar was no longer able to continuously monitor the equatorward expansion of the auroral zone because the auroral oval moved overhead of the radar at this time. By 1750 UT the measurements became dominated by intense scatter (>30 dB) from a target region at the very closest ranges. The bulk of this near-range scatter must have originated in the *E* region. The difficulty in observing scatter from farther ranges may have been, in part, a consequence of heavy absorption of the HF signal in the lower ionosphere on longer propagation paths. This particular radar time series is a classic example of how the capability of the high-latitude SuperDARN radars to continuously monitor ionospheric convection becomes limited during magnetic storms. The need to overcome this limitation was a primary incentive for building the Wallops radar at midlatitudes.

3.1.3. Wallops Radar Measurements

[23] We now turn our attention to Figure 4, which shows data from beam 0 of the Wallops radar between 0900 and 2400 UT on 31 August 2005. This beam direction is aligned east of magnetic north (see Figure 1). The format for Figure 4 is the same as used in Figure 3; the only difference is that the latitude scale runs from 53° to 73°, rather than from 63° to 83° (i.e., 10° lower in magnetic latitude). One particular feature that catches the eye when comparing Figures 3 and 4 is the relatively large amount of groundscatter (grey shading) in the Wallops measurements. This is a general feature of Doppler measurements obtained from Wallops during the daytime, particularly on the morningside. We now compare the Wallops time series (Figure 4) with the Goose Bay measurements during the same time period (Figure 3). However, we must bear in mind that although the two radars are located in the same longitude sector, the beam directions for the data shown in Figures 3 and 4 are not aligned with each other (see Figure 1). From 0900 to 1200 UT the Wallops radar saw very little scatter poleward of 57°; this may have been due to the relatively high operating frequency used during this time (see the frequency legend). At 1200 UT the radar sounding mode identified a band of groundscatter at approximately 64°. The sudden appearance of this groundscatter was most likely in response to a reduction in operating frequency at this time. Over the next 3.5 hours the radar continued to switch frequencies as it searched (in vain) for a substantial target of ionospheric scatter. The effect of varying transmitter frequencies on the HF propagation path for the radar signals can be seen in the changing location of the ground scatter during this period,

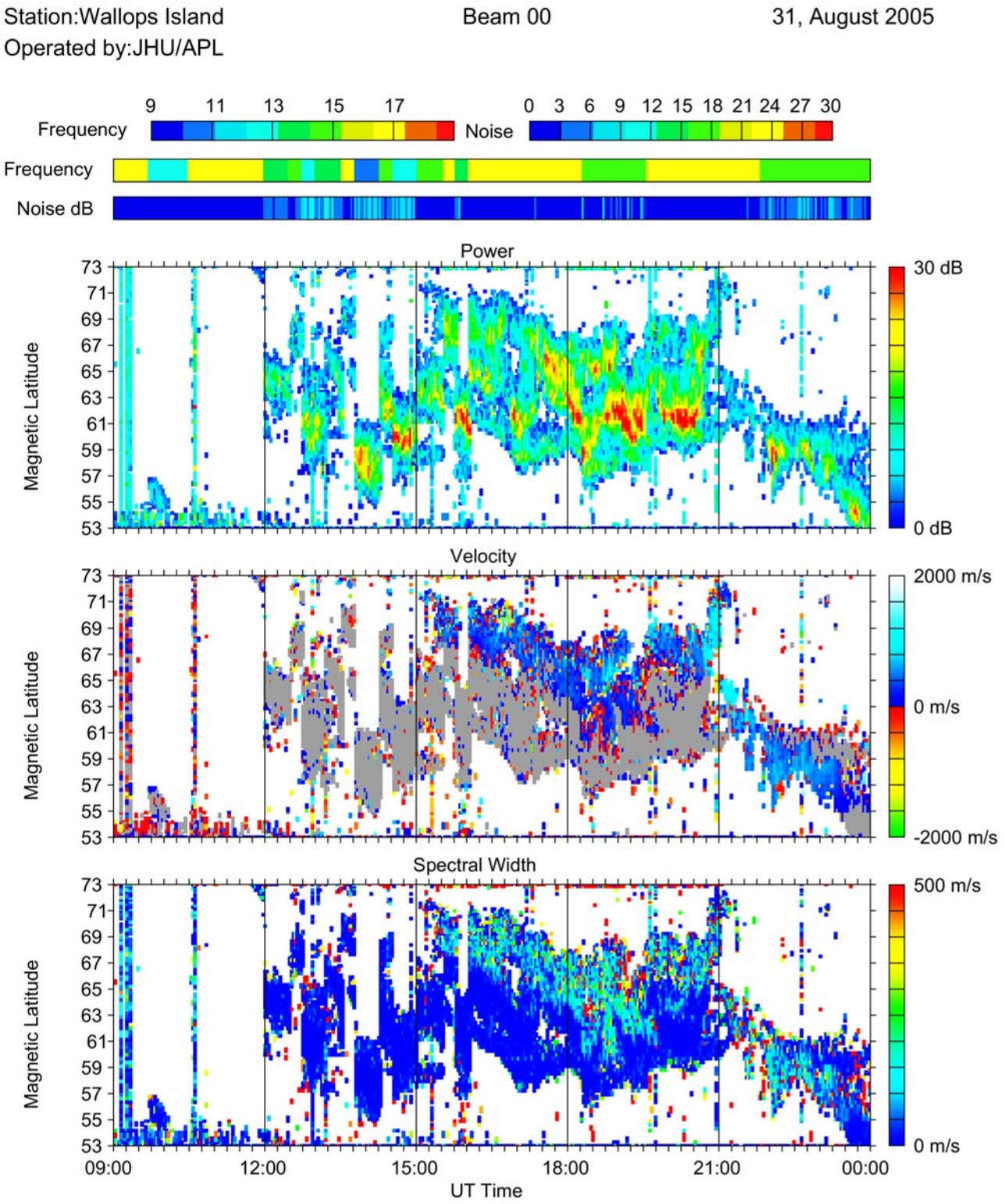

Figure 4. Parameter plot for beam 0 of the Wallops radar between 0900 and 2400 UT on 31 August 2005 (same format as Figure 3).

with lower frequencies producing backscatter at nearer ranges.

[24] At approximately 1520 UT the Wallops radar started to measure substantial ionospheric velocities in a region centered at approximately 70° magnetic latitude. These velocities were predominantly toward the radar, consistent with westward (sunward) flow in the duskside convection cell. By 1532 UT there was a well-defined band of ionospheric scatter in this region. From 1500 to 2400 UT the overall trend was for the ionospheric scatter to move

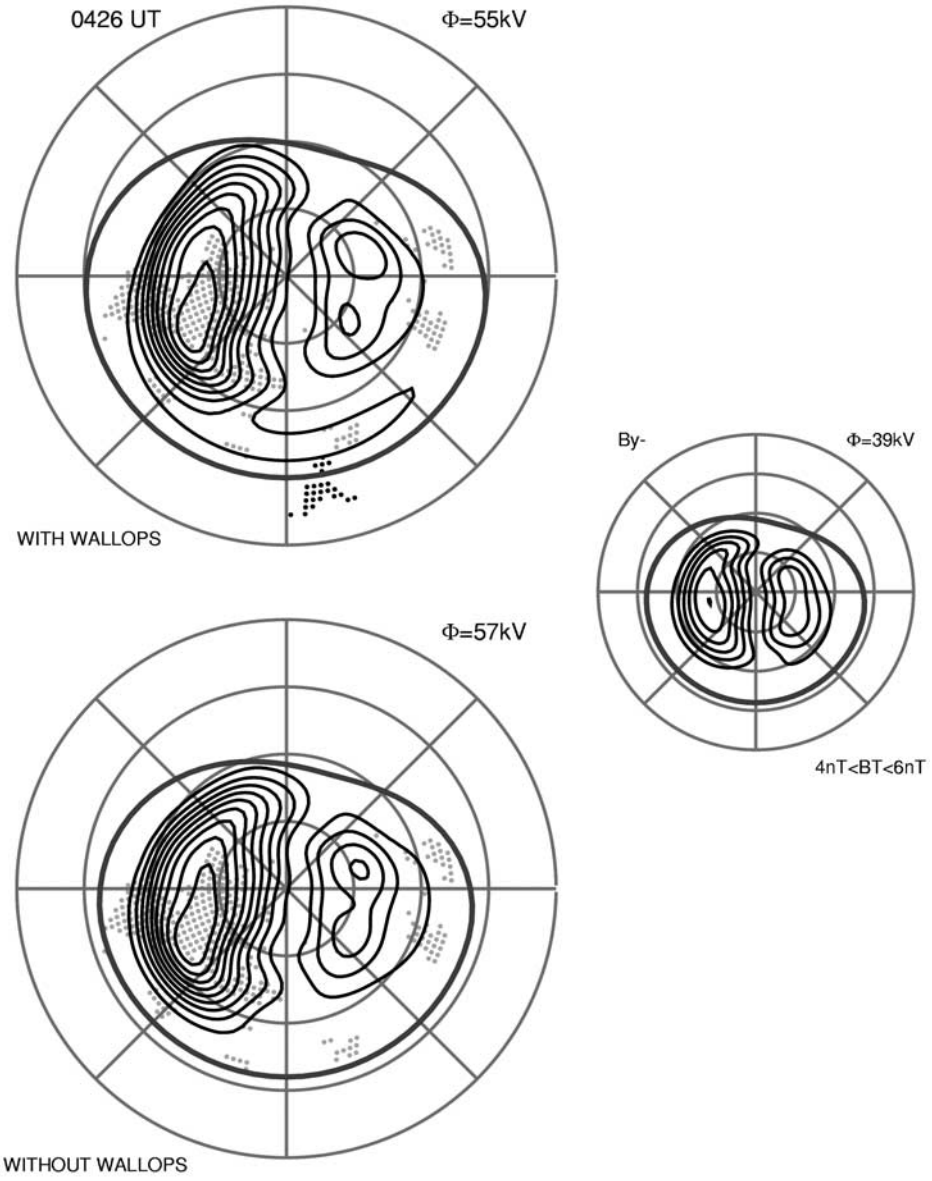

Figure 5. Northern Hemisphere SuperDARN ionospheric convection patterns at 0426 UT on 31 August 2005. The upper (lower) pattern on the left shows the calculated convection with (without) data from the Wallops radar. The smaller pattern on the right shows the background pattern used to constrain the solution in regions of poor data coverage. The format for all three patterns is magnetic latitude versus MLT with magnetic noon directed toward the top and minimum latitude at 50°. Contours of electrostatic equipotential are plotted in black with a spacing of 4 kV. The thick grey contour identifies the lower boundary for the convection at which the potential has been set to zero (the Heppner-Maynard boundary). The value for the cross-polar potential is provided at the upper right of each pattern. For the patterns on the left, grey dots identify gridded Doppler measurements from Wallops; black dots identify measurements from all other Northern Hemisphere SuperDARN radars.

equatorward to lower magnetic latitudes. As was the case for the Goose Bay measurements, the equatorward motion of the scatter can be attributed to two components: (1) a diurnal variation associated with the local-time variation in the auroral zone latitude, and (2) an equatorward expansion of the auroral zone due to the increasing level of geomagnetic activity that started at approximately 1200 UT. (An apparent retreat of the ionospheric scatter to higher latitudes between 1930 and 2100 UT can be attributed to a frequency change that caused the main band of ionospheric scatter to be temporarily obscured by stronger ground scatter; information from the other radars is not consistent with a contraction of the polar cap during this time.) The measurements displayed in Figure 4 show that the Wallops radar was able to continuously observe the high-latitude convection zone from 1500 UT until the end of the day. Recall that the Goose Bay radar was able to observe the onset of geomagnetic disturbance at 1200 UT but lost the ability to

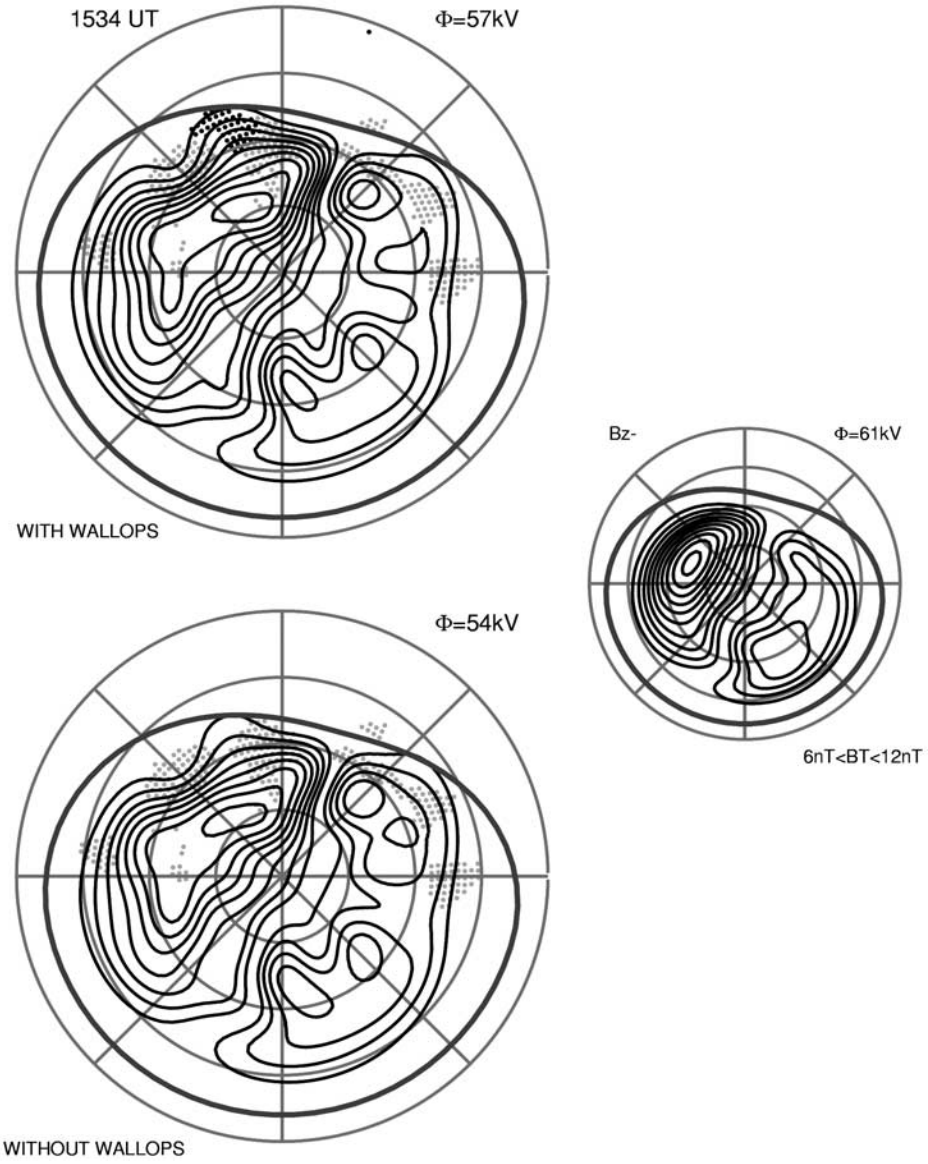

Figure 6. Ionospheric convection patterns calculated from Northern Hemisphere SuperDARN data at 1534 UT on 31 August 2005 (same format as Figure 5).

monitor the expansion of the convection sometime around 1640 UT when the auroral oval became overhead of the radar location. By contrast, Wallops did not observe the onset of the disturbance at 1200 UT, but was able to continuously measure the convection zone once it entered the radar field of view at 1500 UT. In this sense, the Goose Bay and Wallops radars provide complementary measurements over 40° of magnetic latitude in their particular local time sector; together the two radars provide an effective means for monitoring the onset of geomagnetic disturbance at high latitude and the subsequent expansion of storm effects to middle latitudes.

3.1.4. SuperDARN Ionospheric Convection Patterns

[25] In this section we investigate the influence that Wallops measurements had on the calculation of SuperDARN convection patterns during the first few hours of the geomagnetic storm on 31 August 2005. Convection patterns are calculated including and excluding Wallops data, and the differences between the two are examined. The aim of this analysis is to assess the extent to which the measurements from Wallops add new information to the SuperDARN convection patterns. To that end, we will use the cross-polar potential to provide a quantitative measure of the effect that the Wallops data have on the potential patterns; however, we note that the overall coverage of data on this day was not particularly good, so the cross-polar potentials cannot be considered definitive. Indeed, in section 3.1.5 we will present DMSP data identifying important features of ionospheric convection outside the SuperDARN fields of view during this event. In this section we therefore concentrate our efforts on analyzing changes in the morphology of the convection and relative changes in the cross-polar potential that can be attributed to the addition of Wallops data to the SuperDARN data set. Because of the desirability of having simultaneous coverage from Wallops and the higher-latitude radars, the convection

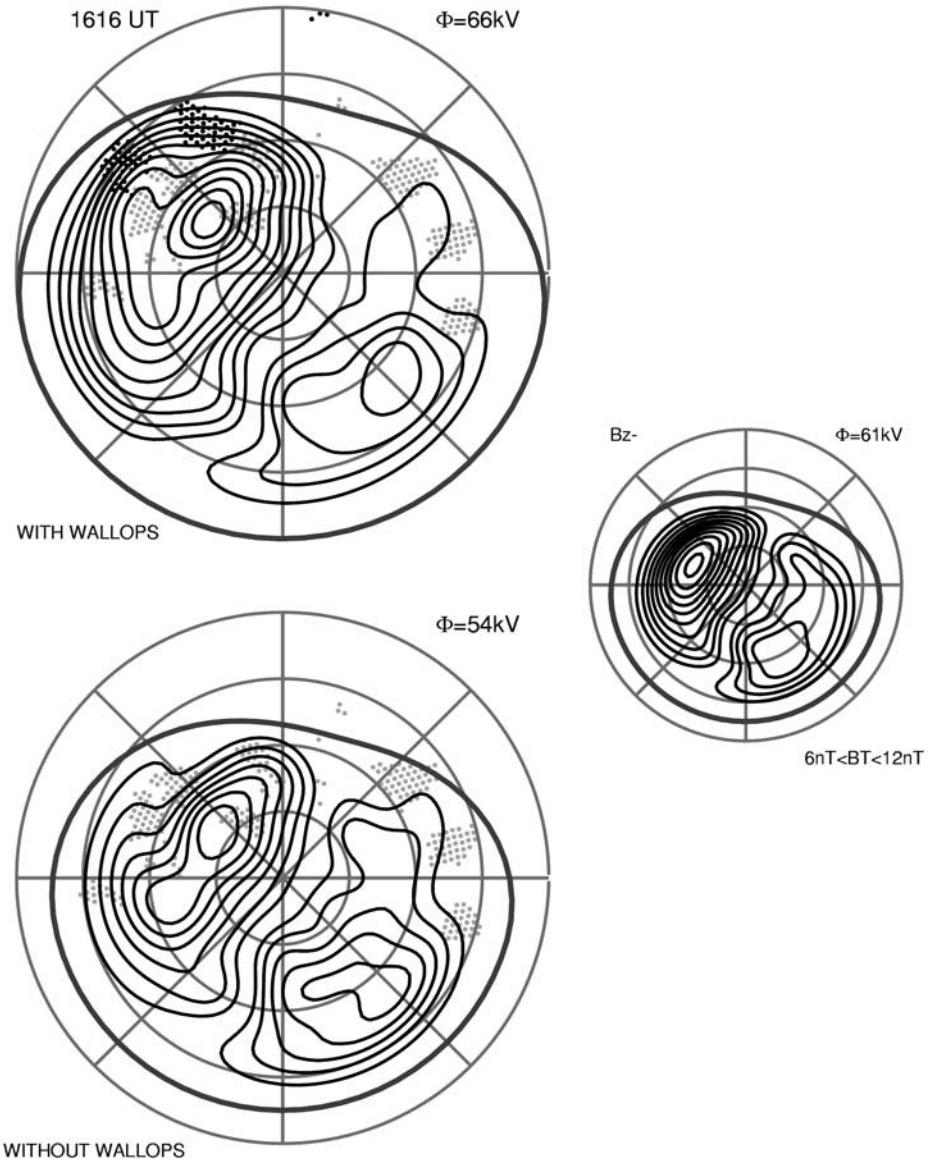

Figure 7. Ionospheric convection patterns calculated from Northern Hemisphere SuperDARN data at 1616 UT on 31 August 2005 (same format as Figure 5).

patterns presented in this section tend to fall in the period 1500–2100 UT when the convection zone had expanded sufficiently to enter the Wallops field of view, but not so much as to expand out of the field of view of the higher-latitude radars.

[26] Figures 5–11 show SuperDARN convection patterns calculated at various times on 31 August 2005. The upper pattern on the left in each figure shows the convection calculated using data from all Northern Hemisphere SuperDARN radars, including Wallops; the lower pattern on the left shows the convection calculated when Wallops data are excluded. The smaller pattern on the right is the *Ruohoniemi and Greenwald* [1996] background pattern that was used to constrain the convection in regions of poor data coverage. Time-shifted ACE spacecraft measurements were used to select the background pattern from the *Ruohoniemi and Greenwald* [1996] statistical patterns. The statistical patterns are binned by the magnitude of the IMF vector in the *Bz-By* plane (B_T) and the corresponding clock angle sector; these parameters are provided at the lower right and upper left, respectively. Each of the convection patterns is presented in Sun-fixed Λ – MLT format using Altitude Adjusted Corrected Geomagnetic (AACGM) coordinates [*Baker and Wing*, 1989]. The magnetic pole is at the center of the pattern; magnetic noon is directed up the page and the outer circle identifies the minimum latitude at 50°. Contours of electrostatic equipotential are plotted with a contour spacing of 4 kV. The thick grey contour encompassing the potential contours identifies the Heppner-Maynard (HM) boundary at which the potential has been set to zero. The start time of each 2-min scan is provided at the upper left of each of the patterns on the left; the cross-polar potential is given at the upper right of each pattern. Gridded line-of-sight velocity measurements from 10 Northern Hemisphere SuperDARN radars contributed to the calculation of each of the patterns on the left: grey dots identify measure-

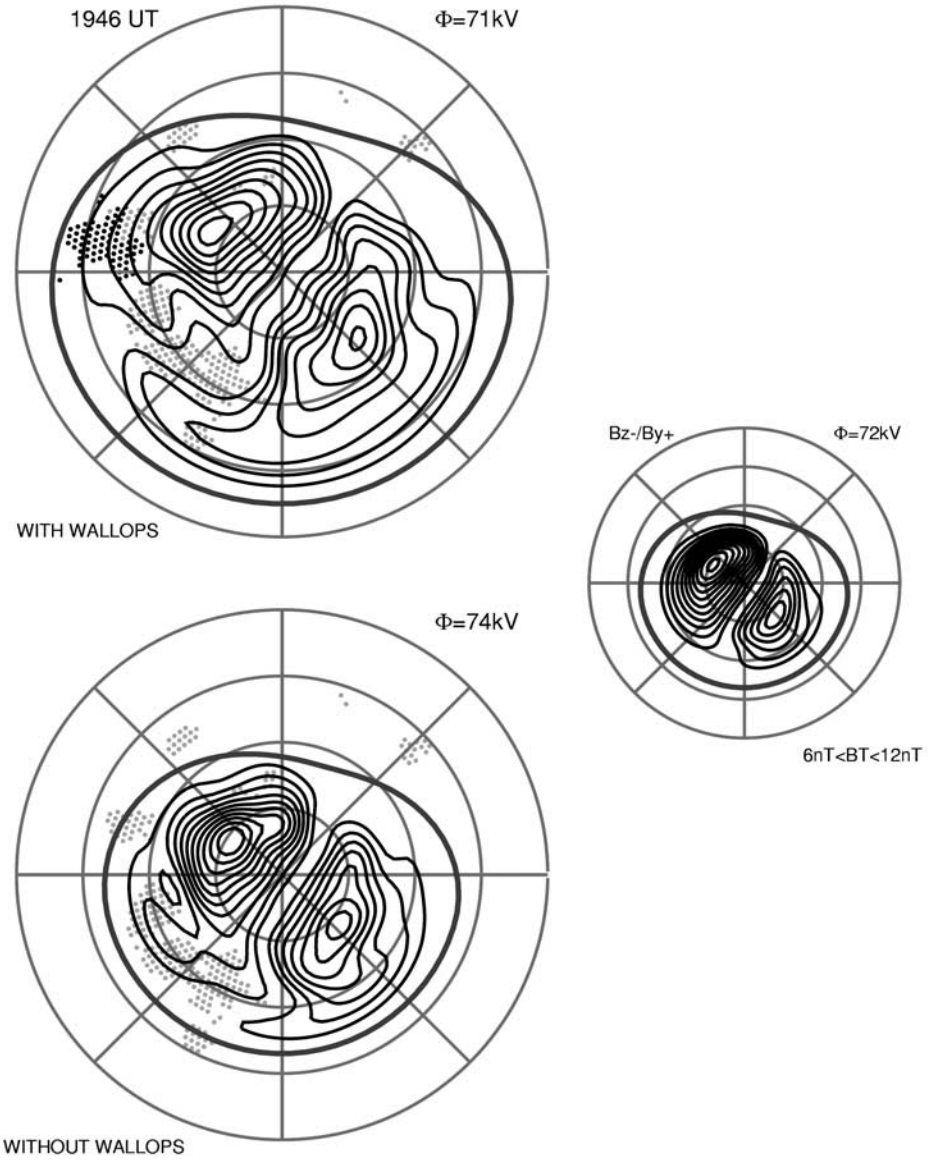

Figure 8. Ionospheric convection patterns calculated from Northern Hemisphere SuperDARN data at 1946 UT on 31 August 2005 (same format as Figure 5).

ments from one or more of the nine high-latitude SuperDARN radars; black dots identify measurements from Wallops. A direct comparison between the upper and lower patterns on the left provides a straightforward characterization of the impact that Wallops data have on the determination of SuperDARN ionospheric convection patterns. Comparing the patterns on the left with the pattern on the right provides an indication of the extent to which the convection patterns are defined by the Doppler measurements, rather than the background pattern. We now discuss each pair of convection patterns in more detail.

[27] Figure 5 shows the three interpretations of the ionospheric convection at 0426 UT, prior to the onset of the geomagnetic storm when $Kp = 2^+$. By comparing the two patterns on the left with the smaller background pattern on the right, it can be seen that the overall strength of convection at this time was stronger than what was predicted by the IMF statistical model alone; the convection in the duskside cell was particularly strong. At this time the Wallops radar was measuring Doppler velocities in the midnight sector (i.e., the black dots in upper left pattern). The Wallops measurements are largely consistent with those from the other radars, but they do produce two significant changes in the morphology of the convection. First, the HM boundary in the upper left pattern is at slightly lower latitude (60° rather than 62°). This distinction can be attributed to the fact that the Wallops measurements provide a better characterization of the dropoff in the magnitude of the convection velocity at the equatorward boundary of the high-latitude convection. Second, the measurements from Wallops alter the morphology of the convection in the midnight sector, producing an elongated tongue of convection that extends from premidnight to early morning and is characterized by westward convection at the lowest lati-

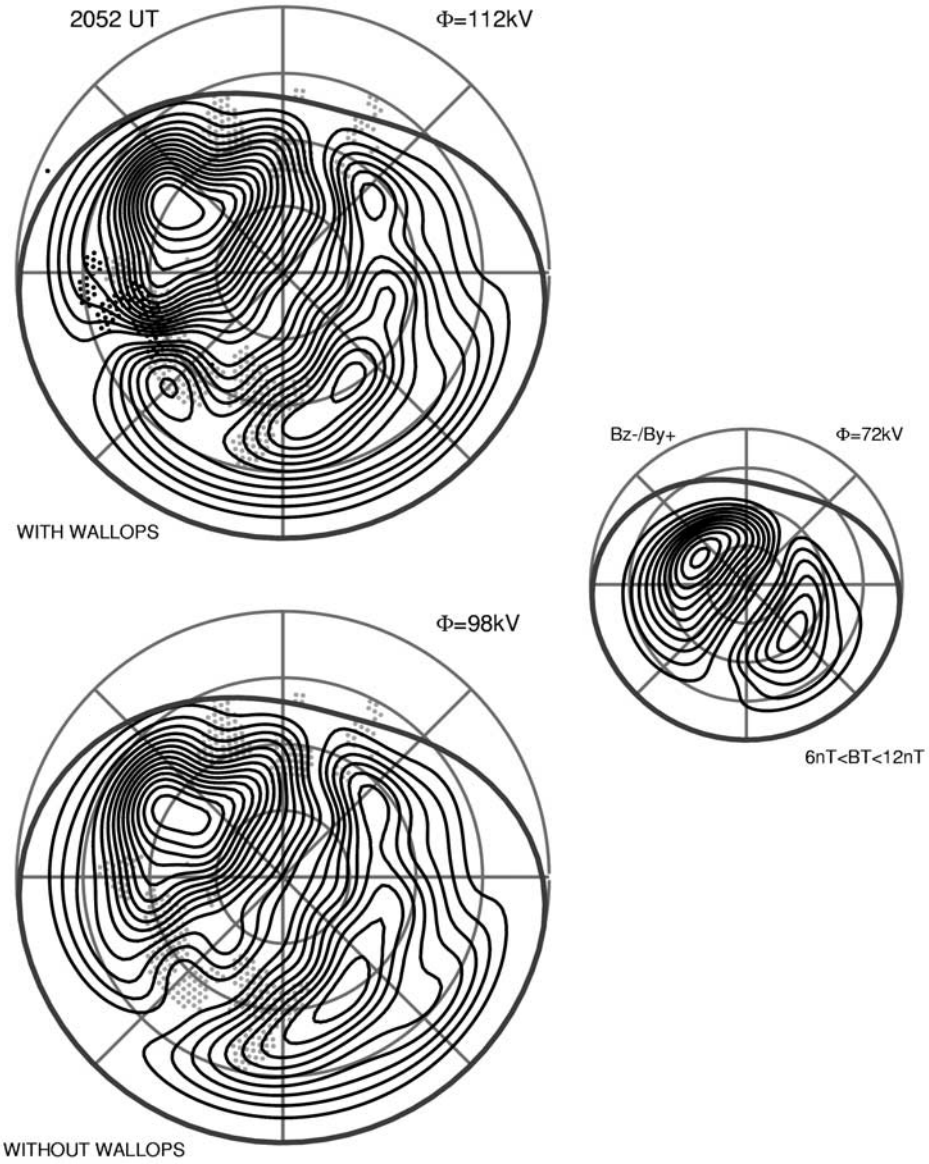

Figure 9. Ionospheric convection patterns calculated from Northern Hemisphere SuperDARN data at 2052 UT on 31 August 2005 (same format as Figure 5).

tudes. These changes to the morphology of the convection pattern produce a small reduction in the cross-polar potential (55 kV versus 57 kV).

[28] Figure 6 shows convection patterns at 1534 UT. At this particular time, the IMF had been southward for approximately 3 hours, the polar cap area was expanding, and the high-latitude convection had just entered the Wallops field of view but was still confined to the farthest range gates (see Figure 4). The black dots in the upper left pattern show that the measurements from Wallops filled a small gap in the coverage of the higher-latitude radars in the postnoon sector but did very little to extend the coverage in latitude. The cross-polar potential for the upper left pattern is slightly higher than it is for the lower left pattern (57 kV versus 54 kV); this difference can be attributed in part to the fact that the HM boundary is pushed to slightly lower latitude in the upper left pattern (53° versus 54°), allowing a larger amount of plasma to enter the polar cap. More generally, the morphology of the convection in both patterns is essentially similar in the local time sector where the Wallops measurements were obtained. In particular, the bulge in sunward convection contours seen in the upper left pattern in the vicinity of the Wallops measurements is correctly implied in the lower left pattern when Wallops measurements are excluded. This implies that the measurements from the high-latitude SuperDARN radars were largely successful at defining the convection pattern in the afternoon sector at this particular time without the need for measurements from Wallops. To be sure, the Wallops measurements provide additional constraints on the convection pattern, but these constraints are no more significant at this particular time than those provided by the data from each of the other radars.

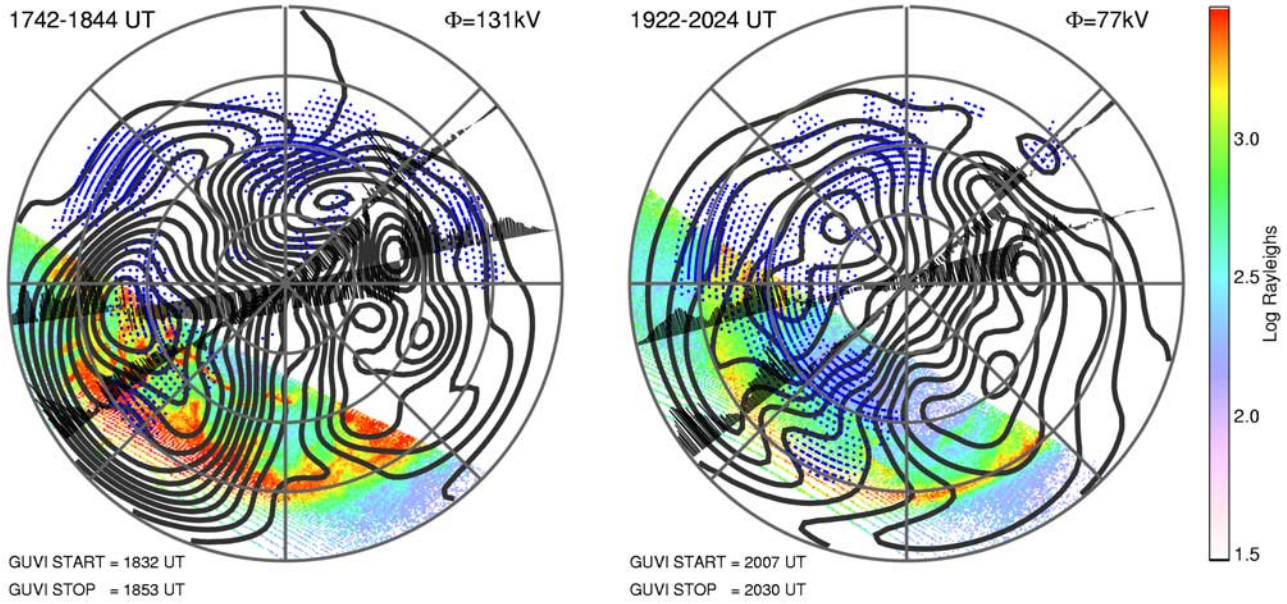

Figure 10. Ionospheric convection patterns calculated for (left) 1742–1844 UT and (right) 1922–2024 UT from F13/F15 DMSP driftmeter and SuperDARN data overlain on TIMED GUVI images. Each panel is presented in MLAT-MLT format with the lower latitude boundary at 50° and magnetic noon at the top. Contours of electrostatic equipotential are plotted in black with a spacing of 4 kV. Blue dots identify locations of gridded SuperDARN measurements; black lines show the location and strength of cross-track DMSP driftmeter measurements. The DMSP F13 satellite is in the 1900–0700 MLT orbit; F15 is in the 2000–0800 MLT orbit. The value for the DMSP-SuperDARN cross-polar potential is provided at the upper right of each panel. The time period over which the GUVI swath was obtained is shown at the bottom left.

[29] Figure 7 shows convection patterns at 1616 UT when the polar cap had expanded equatorward to such an extent that the ability of the high-latitude radars to observe the full extent of the convection was becoming compromised. At this time, Wallops was measuring strong sunward flows across 2–3 hours of local time in the afternoon sector. In comparing the upper and lower left patterns it is apparent that the high-latitude radars are missing a substantial component of the convection in the afternoon sector seen by Wallops. As a consequence, the HM boundary is estimated to be significantly more poleward in the lower pattern (55°) than it is in the upper pattern (50°). This shift in the latitude of the HM boundary, combined with the stronger flows measured by Wallops, increases the cross-polar potential from 54 kV to 66 kV. Put another way, the Wallops measurements add potential contours to the convection pattern at lower latitudes.

[30] Figure 8 shows convection patterns at 1946 UT when the Wallops radar was obtaining measurements in the dusk sector. The difference between the HM boundaries in this case is very large: 55° in the upper left pattern and 63° in the lower left pattern. This discrepancy can be attributed to two problems associated with near-range measurements from the higher latitude radars: (1) Some of the returns originate in the *E* region and so the measured velocities are lower than the $\mathbf{E} \times \mathbf{B}$ convection velocity, and (2) the nearest range gates have poleward pointing azimuths that provide limited information about the zonal component of the flows. Both problems conspire to produce measurements that underestimate the true strength of the convection and place the HM boundary at higher latitudes than it should be. Despite these problems, it is interesting to note that the cross-polar potential in the upper left pattern is actually smaller than it is in the lower left pattern. This can be explained by the fact that the coverage of the radars was not sufficient to conclusively define the arrangement of potential contours at high latitude. Because of the sparse spatial coverage the potential fitting algorithm can accommodate the Wallops measurements in such a way that it does not add additional contours to the convection pattern at lower latitudes, but instead provides an alternative closure for the existing contours at higher latitudes where there are no data constraints.

[31] Figure 9 shows the ionospheric convection at 2052 UT on 31 August 2005. At this time the Wallops radar was making measurements in the dusk sector and the SuperDARN radars were in a position to simultaneously measure the flows entering and exiting the polar cap on the dayside and nightside, respectively. The value for the upper left pattern in Figure 9 is the highest measured by the SuperDARN radars during this particular event. It is interesting to note that the cross-polar potential in the upper left pattern is significantly elevated over the pattern at bottom left (112 kV versus 98 kV) despite the fact that the HM boundary in both patterns is at 50°. This suggests that the increased cross-polar potential for the upper left pattern did not result from an increase in spatial coverage to lower latitudes, but rather from an increase in the number of high-velocity measurements. In other words, the impact of the measurements provided by the Wallops radar at this particular time is

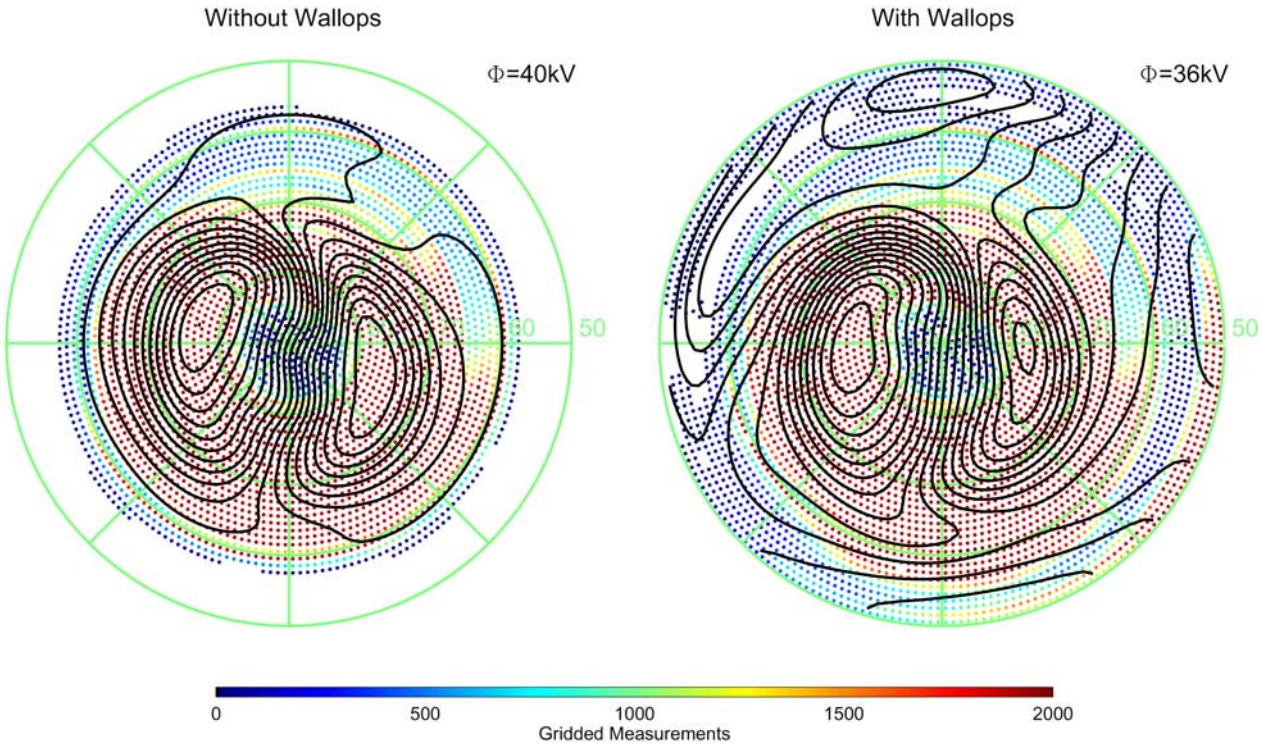

Figure 11. Average patterns of Northern Hemisphere ionospheric convection calculated from SuperDARN data collected during periods of weak geomagnetic activity ($Kp \leq 3$) between June 2005 and April 2006. The panel on the right (left) shows the convection calculated with (without) data from the Wallops radar. The format is the same as used in Figures 4–10; the contour spacing is 2 kV; the cross-polar potential is provided at the upper right. Colored dots show how many gridded Doppler measurements contributed to the patterns at a given location according to the scale provided along the bottom.

similar to that which might be expected from the addition of any new radar, at high or middle latitudes. This was also the case in Figure 6.

3.1.5. DMSP-SuperDARN Convection Patterns and TIMED GUVI Images

[32] The analysis presented in section 3.1.4 showed the incremental changes that result when Wallops data are included in the calculation of SuperDARN ionospheric convection patterns for the 31 August 2005 event. However, as stated previously, the spatial coverage provided by SuperDARN during this interval was not particularly good and so the convection patterns in Figures 5–9 cannot be considered definitive. To obtain a more comprehensive picture of this particular event, it is necessary to incorporate other data sets into the convection analysis, particularly at middle latitudes in longitude sectors removed from the Wallops radar; and also at the highest latitudes of the polar cap. The Ion Drift Meter (IDM) instruments aboard the polar orbiting DMSP (Defense Meteorological Satellite Program) spacecraft are ideal data sets to provide additional constraints on the convection in these regions. Very briefly, the IDM design employed by DMSP was modified only slightly from that originally used on the DE and AE satellites [*Heelis et al.*, 1981]. IDM is basically a modified Faraday cup that measures the bulk flow of plasma in the horizontal direction at right angles to the direction of spacecraft motion. Incorporating DMSP drift meter data into the SuperDARN convection analysis is reasonably straightforward because both techniques measure the drift of plasma in the Earth's *F* region ionosphere. Furthermore, there is an overwhelming incentive to combine these two data sets because they are complementary in many ways. DMSP IDM measurements are obtained at all latitudes and therefore provide excellent information about the equatorward extent of the convection; however, the suite of DMSP spacecraft samples only a few discrete local times with orbital periods of approximately 104 min. By contrast, SuperDARN has the ability to provide extended local time coverage at auroral latitudes and can monitor convection dynamics on timescales of 1–2 min; however, the spatial coverage of SuperDARN measurements is variable and highly dependent on geophysical conditions. By combining the two data sets we can reinforce their collective strengths while at the same time offsetting their individual limitations.

[33] To aid the interpretation of SuperDARN-DMSP convection patterns, it is also desirable to have measurements of auroral activity so that the equatorward edge of the auroral oval can be identified and the convection features can be separated into auroral and subauroral components. The GUVI (Global Ultraviolet Imager) instrument aboard the TIMED (Thermosphere-Ionosphere-Mesosphere Energetics and Dynamics) spacecraft can provide this type of information [*Christensen et al.*, 2003]. TIMED GUVI is a cross-track scanning spectrometer that measures auroral

emission at five ultraviolet ''colors'': H (121.6 nm), O (130.4 nm), O (135.6 nm), LBHS (140–150 nm), and LBHL (165–185 nm). The orbital period of the TIMED spacecraft is approximately 98 min, and the GUVI swath is typically 3000 km wide.

[34] On 31 August 2005 the IDM instruments on the DMSP F13 and F15 spacecraft were both functioning nominally (unfortunately, the IDM on F14 suffered a failure in September 1999 and subsequent data are corrupted in daylight). To combine DMSP IDM data with SuperDARN measurements, it is first necessary to widen the window of time over which plasma drift data are ingested into the convection fitting algorithm. This ensures that the DMSP measurements cover as much of the polar region as possible. In this case, by widening the window to 62 min IDM measurements from both F13 and F15 can be included in the calculation of a single convection pattern. Figure 10 shows DMSP-SuperDARN convection patterns calculated during two time periods: 1742–1844 UT (the pattern on the left) and 1922–2024 UT (the pattern on the right). Each panel is presented in MLAT-MLT format with the lower-latitude boundary at 50° and magnetic noon at the top. Contours of electrostatic equipotential are plotted in black with a spacing of 6 kV. Blue dots identify the locations of gridded SuperDARN measurements; black lines show the location and strength of DMSP IDM measurements: F13 in the 1900–0700 MLT orbit and F15 in the 2000–0800 MLT orbit. The value for the DMSP-SuperDARN cross-polar potential is provided at the upper right of each panel. Each convection pattern is overlain on a swath of LBHL brightness obtained by TIMED GUVI colored according to the color bar at the right. The time period over which the GUVI swath was obtained is shown at the bottom left of each convection pattern.

[35] When the convection patterns in Figure 10 are compared with those presented in the previous section (particularly Figures 8 and 9), one can see a number of important differences, some of which can be attributed to the additional constraints provided by DMSP in locations not sampled by SuperDARN; others are associated more with the fact that the patterns in Figure 10 have been calculated using data collected over a time period much longer than 2 min (i.e., approximately 1 hour). When one compares Figure 9 with the right panel of Figure 10 it can be seen that the DMSP measurements refine the structure of the dawn cell in the prenoon sector and produce substantial changes in the morphology of the dusk cell in the postdusk sector. In particular, there is a pronounced two-peak structure to the latitudinal profile of sunward convection measured by both DMSP spacecraft between 1800 and 2100 MLT over two consecutive passes. The GUVI LBHL swaths show that the second convection peak at lower latitudes is equatorward of the auroral oval (i.e., subauroral). This is a classic example of the subauroral polarization stream (SAPS) [*Foster and Burke*, 2002]. Although there is some evolution in the location and strength of the SAPS between the two convection patterns (particularly in the F13 data), it is clear that it is a long-lived and relatively stable feature.

[36] This example demonstrates the potential benefits that can be gained by using multiple data sets to calculate ionospheric convection patterns. In this case, the SAPS feature was long-lived and the inclusion of DMSP data has undoubtedly improved the depiction of the global convection pattern. However, the need to average over an extended period (~1 hour) to capture a sizeable set of DMSP measurements has also resulted in a washing out of much of the detailed structure in the convection that is transient on shorter timescales. Building more HF radars at middle latitudes would reduce this problem and help gain a more accurate view of the instantaneous convection associated with SAPS channels. There are two reasons why the Wallops radar did not identify the SAPS during this particular event interval: (1) The radar was in the wrong local time sector (i.e., predusk), and (2) the radar was operating with a limited field of view that did not provide optimum spatial coverage at the lowest possible latitudes (see Figure 1). *Oksavik et al.* [2006] examined a different event in which the Wallops radar was in a good position to monitor temporal changes in a SAPS channel with unprecedented temporal resolution. The ability of the Wallops radar to monitor SAPS channels improved significantly in January 2006 when the field of view was widened (see Figure 1).

3.2. Average Convection Patterns

[37] The convection patterns presented in the previous sections showed that Doppler measurements from the Wallops radar provide important additional information about midlatitude convection, particularly during disturbed conditions. However, the statistical significance of the Wallops data in the convection patterns calculated for the 31 August 2005 event is, to some extent, overwhelmed by the larger amount of measurements from the other radars at high latitude. It is worthwhile to investigate the measurements from the Wallops radar in a manner that puts them on a more equal statistical footing with the data from the other radars. Eventually, it will be possible to construct new statistical models of midlatitude ionospheric convection based on the Wallops data set and ordered by geomagnetic activity and interplanetary conditions, but a proper treatment will require good statistics at all local times and over a wide range of geomagnetic activity levels. The small data set accumulated from the Wallops radar at the current time does not allow this type of comprehensive statistical analysis. We instead focus our efforts here on producing a crude characterization of midlatitude convection for ''quiet'' and ''disturbed'' conditions, based on the *Kp* magnetic index. We stress that these results should be considered preliminary and will be expanded upon in the future as the Wallops data set increases in size and geomagnetic complexity over the next few years. Figures 11 and 12 show average patterns of ionospheric convection calculated using measurements from all 10 Northern Hemisphere SuperDARN radars operating between June and September 2005. Figure 11 shows the average convection for quiet geomagnetic conditions ($Kp \leq 3$); Figure 12 shows the average convection for disturbed conditions ($Kp \geq 3$). These particular *Kp* bins were chosen to maximize data coverage while providing the opportunity to make qualitative comparisons with results obtained from other studies of midlatitude convection [e.g., *Heelis and Coley*, 1992; *Buonsanto and Witasse*, 1999]. The pattern on the right in each figure shows the average convection calculated using all available data, including Wallops; the pattern on the left shows the average convection when the Wallops data are excluded. The format for the

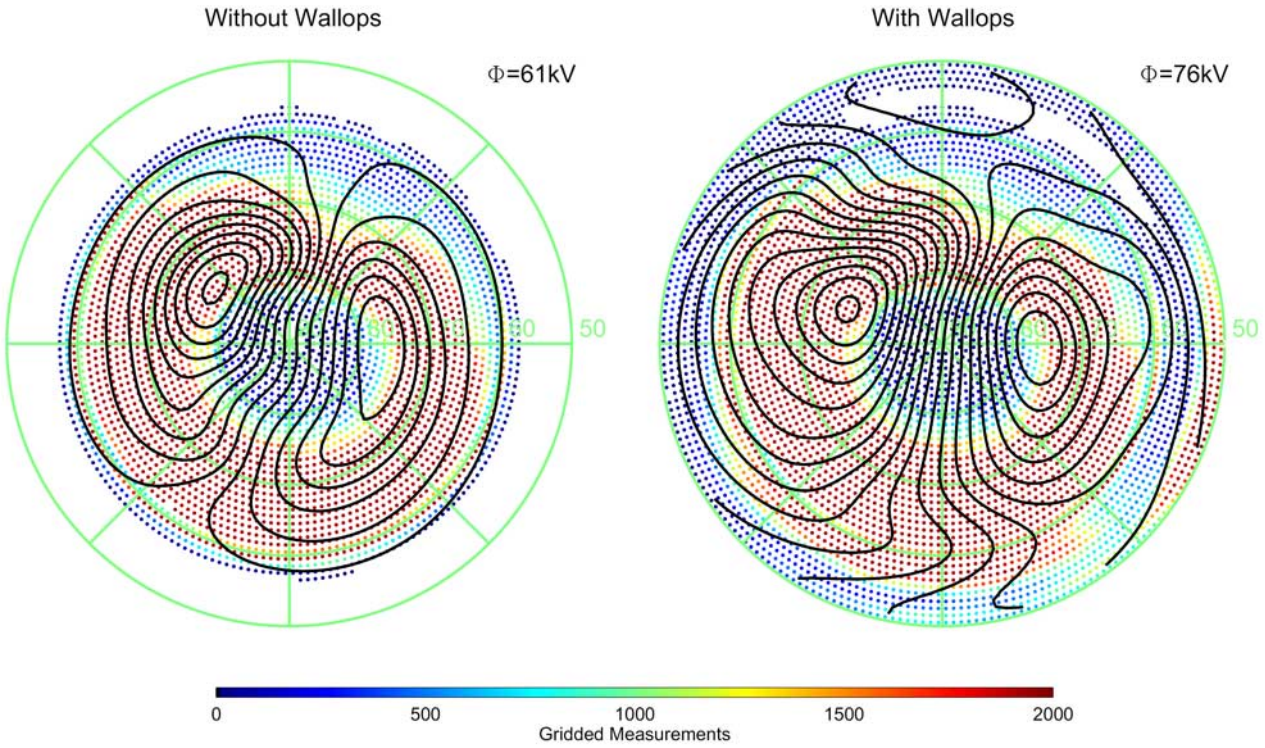

Figure 12. Average patterns of Northern Hemisphere ionospheric convection calculated from SuperDARN data collected during periods of increased geomagnetic activity ($Kp \geq 3$) between June 2005 and April 2006. The format is the same as used in Figure 10, except the contour spacing is 4 kV.

convection patterns is the same as used in Figures 5–9. The value of the cross-polar potential for each pattern is provided at the upper right. Colored dots identify how many gridded Doppler measurements contributed to the patterns at a given location according to the color scale provided along the bottom. The contour spacing is 2 kV in Figure 11 and 4 kV in Figure 12. Each figure provides a straightforward characterization of the impact that Wallops data have on the determination of average convection patterns during weak geomagnetic activity (Figure 11) and during disturbed conditions (Figure 12).

[38] Before we discuss the features of Figures 11 and 12 it is first appropriate to describe in more detail how the convection patterns were derived. Perhaps the simplest method would have been to feed all gridded line-of-sight velocity measurements obtained for the particular *Kp* conditions into the spherical harmonic fitting algorithm. This is the approach that was used for the event study in section 3.1.4. The problem with using this approach for a statistical study, however, is that data obtained above 60° magnetic latitude carry a far larger statistical weight in the final solution because of the better coverage provided by the radars at higher latitudes. (For example, the number of Doppler measurements between 60° and 70° MLAT used to calculate the pattern on the right in Figure 12 is 1,369,823; the corresponding number between 50° and 60° MLAT is 58,978.) To reduce this sampling bias, the gridded line-of-sight Doppler velocities have been preprocessed to produce an estimate for a single ''characteristic'' ionospheric velocity vector at each MLAT/MLT location for the appropriate geophysical conditions. The magnitude and direction of the characteristic velocities were calculated by fitting all of the line-of-sight Doppler velocity measurements at a particular location and in a particular *Kp* bin to a cosine function of the measured line-of-sight magnetic azimuths. This approach is similar to that used in other statistical studies of ionospheric convection based on ground-based radar measurements [e.g., *Holt et al.*, 1987]. This preprocessing produced a large compression in the number of vectors input to the spherical harmonic fitting algorithm. (For the pattern on the right in Figure 12 the number of velocity inputs was reduced from 2,616,883 individual line-of-sight Doppler velocities to 4812 characteristic velocity vectors.) However, there still remains the issue of how to weight the characteristic velocity vectors in the fitting algorithm. In section 3.1.4 the inverse of the measured Doppler velocity error was used. For the average patterns, we have two choices for an appropriate velocity error: (1) the numerical average for the ensemble of line-of-sight velocity errors obtained at that MLAT/MLT location or (2) the variability in the magnitude of measured line-of-sight velocities resolved along the characteristic velocity direction. We have chosen to use the larger of these two velocity errors at each location. It should also be stressed that no vectors from a background pattern (i.e., statistical model) have been used in the calculation of the patterns in Figures 11 and 12.

[39] We now discuss the features in Figures 11 and 12 in more detail with the goal of characterizing the impact that data from the Wallops radar have on the calculation of average ionospheric convection patterns as a function of geomagnetic activity level and for gaining insight into the

nature of convection at lower latitudes. Comparing the two patterns in Figure 11 shows how Wallops data provide increased detail of the convection between 50° and 60° invariant latitude during quiet conditions: westward across the nightside; eastward at dawn; northward just prior to dawn; and southward prenoon. Near dusk there is a reversal from eastward flows near 50° to westward flows above 60°. This picture of the midlatitude ionospheric convection merges naturally with the stronger two-cell convection seen at higher latitudes but produces a slightly smaller value for the cross-polar potential. In the midnight sector the addition of the two-cell convection to westward convection produces a tongue of convection that protrudes from the dusk cell across midnight into the early morning hours and the outflow region moves to later local times (i.e., the outflow streamlines become kinked). In addition, the color coding gives an impression of the rates of ionospheric scatter seen by the Wallops radar as functions of MLAT and MLT during quiet conditions. The majority of measurements obtained from Wallops are on the nightside; between 55° and 60° the distribution is centered around midnight. There is also a higher probability of obtaining scatter on the dawnside.

[40] Figure 12 shows average convection patterns calculated for periods when $Kp \geq 3$ in the same format as used in Figure 11. It can be seen that the Wallops measurements provide important new constraints on the midlatitude convection below 60° during periods of increased geomagnetic activity. Without Wallops data (left pattern) the fitting algorithm is forced to infer the pattern of return convection below 60° by matching the strength and direction of flows entering and leaving the polar cap at higher latitudes on the dayside and nightside, respectively. Under these circumstances the amount of sunward convection in the auroral zone is underestimated. When Wallops data are included in the convection analysis the average cross-polar potential increases from 61 to 76 kV, an increase of 25%. This is a substantial difference, especially since it can be argued that the lower bound for the geomagnetic activity at $Kp = 3$ does not represent particularly disturbed conditions. Indeed, preliminary indications show that for periods in which $Kp \geq 5$ the increase in cross-polar potential may be as high as 30–40% (not shown). Also apparent in Figure 12 is the manner in which Wallops measurements alter the morphology of the convection in the sunward return flow regions, particularly in the midnight sector where there is a strong westward component to the convection equatorward of 60°, which adds a kink to the streamlines of outflow from the polar cap. This particular feature, and some of the others displayed in Figures 11 and 12, will be discussed in more detail in the next section and compared with results obtained from previous studies of midlatitude convection.

4. Discussion

[41] The primary motivation for building the Wallops radar at middle latitudes was to improve the ability of SuperDARN to measure ionospheric convection during periods of increased geomagnetic activity (e.g., magnetic storms). The results presented in this paper demonstrate that this goal has been achieved in the longitude sector covered by the Wallops field of view. On 31 August 2005 the measurements from Goose Bay and Wallops allowed continuous monitoring of ionospheric convection over the Canadian maritime provinces during the first few hours of a magnetic storm: Goose Bay measured the onset of geomagnetic disturbance at high latitudes at approximately 1200 UT; Wallops missed the onset but was able to monitor the equatorward expansion of the convection for many hours after Goose Bay became ineffective at 1730 UT. Both radars were able to measure the convection simultaneously during the period 1500–1730 UT. The analysis of convection patterns during the onset of the storm (Figures 5–9) provides additional confirmation that the Wallops radar has improved the effectiveness with which SuperDARN can monitor ionospheric convection during periods of increased geomagnetic disturbance. However, DMSP drift meter data identified a SAPS channel that was outside the field of view of the Wallops radar. When Wallops measurements are included in the calculation of average convection patterns for quiet and disturbed conditions ($Kp \geq 3$), the kinking of streamlines in the outflow region becomes accentuated and the average cross-polar potential is increased by 25%. Much of this increase in potential can be attributed to the fact that Wallops provides a better characterization of the equatorward extent of the convection pattern. *Burke et al.* [1998] found that during magnetic storms a substantial component of the potential in the dusk cell was associated with subauroral drifts. The DMSP drift meter data presented in Figure 10 show that this was the case for the event on 31 August 2005.

[42] It is appropriate to compare the average convection pattern for weak geomagnetic activity shown in Figure 11 with the average behavior of quiet time drifts measured at middle latitudes by the Millstone Hill incoherent scatter radar [*Buonsanto et al.*, 1993; *Buonsanto and Witasse*, 1999] and the DE 2 spacecraft [*Heelis and Coley* 1992]. *Buonsanto and Witasse* [1999] found that during quiet times the drifts at Millstone Hill are generally northward in the early morning, turn abruptly southward near local noon, and then turn northward again sometime in the evening. Zonal drifts were found to be eastward during the day and westward at night; these features were explained in terms of the dynamo action of winds in the *E* and *F* regions. *Heelis and Coley*, [1992] used DE 2 data to identify dawn-dusk asymmetries in the zonal component of midlatitude convection during quiet times. On the dawnside they identified a clear separation between eastward auroral flows at high latitudes and westward neutral dynamo flows at middle latitudes. On the duskside the flows in both regimes were westward, so there was no obvious transition between the two regimes, and the flows tended to be stronger. The findings of these previous studies are largely consistent with the convection pattern shown in the right panel of Figure 11. Furthermore, Figure 11 shows how these features of the convection at middle latitudes merge with the two-cell convection at higher latitudes. However, one major distinction is that the magnitudes of the average midlatitude drifts seen by Wallops during quiet times are larger than those identified in these previous studies by a factor of approximately 1.5–2. There are two possible explanations for this distinction. First, the *Kp* bins for weak activity used in the previous studies were much more restrictive than the one used here. Second, it is likely that the Wallops measurements used to calculate the average drift velocities in

Figure 11 are biased to higher magnitudes because of incorrect groundscatter determination. The criteria currently used to discard Doppler measurements as being groundscatter in SuperDARN measurements are the following: The magnitude of the Doppler velocity is <35 m/s and the spectral width is <10 m/s. This criterion has worked well at high latitudes where the ionospheric velocities tend to be large, even during quiet conditions. However, at middle latitudes under quiet conditions, ionospheric velocities might often have magnitudes less than this velocity threshold. It is therefore likely that a large fraction of the low velocities discarded from the Wallops data set for being contaminated by groundscatter were actually low-magnitude ionospheric velocities. This finding suggests that groundscatter determination is an issue that needs to be revisited for the Wallops data set.

[43] When geomagnetic conditions become more disturbed, the neutral dynamo electric fields at middle latitudes become enhanced and are augmented by auroral electric fields, penetration electric fields, and SAPS electric fields [*Blanc and Richmond*, 1980]. Distinguishing between these influences can be difficult. *Heelis and Coley* [1992] presented a schematic of the various magnetospheric contributions to the east-west ion drift as a function of local time. In that picture, an expansion of the auroral electric fields to middle latitudes is expected to produce a symmetric local time distribution of the zonal drift with westward drifts premidnight and eastward drifts postmidnight. The other magnetospheric sources generally produce westward flows across midnight. The dawn-dusk symmetry of the features shown in the midlatitude convection displayed in Figure 12 is therefore consistent with auroral electric fields being the dominant influence during disturbed times. This was also the case during the first few hours of the storm on 31 August 2005 (section 3.1) when the equatorward expansion of auroral electric fields was measured directly by Goose Bay and Wallops. Undoubtedly, some fraction of the measurements from Wallops that contributed to Figure 12 are also SAPS-related and due to penetration electric fields. Understanding the precise partitioning of disturbance electric fields between these three categories is an important focus of current study with the Wallops data set that requires ancillary information from other data sets. In Figure 10, TIMED GUVI auroral imaging was used to classify convection measured by DMSP as subauroral. In a similar fashion, *Oksavik et al.* [2006] used TIMED GUVI and low-altitude precipitation measurements to identify a SAPS channel in Wallops data. Extending this type of correlative multi-instrument analysis to the entire database of Wallops measurements is a much larger task that is beyond the scope of the present paper. Similarly, identifying penetration electric fields is even more challenging because it requires simultaneous measurements of electric fields at middle and high latitudes to be compared with measurements in the interplanetary medium.

[44] One of the most striking results obtained from including Wallops data in the calculation of average SuperDARN convection patterns is the accentuated kinking of streamlines in the nightside outflow region. This feature is sometimes referred to as the Harang discontinuity (HD), which was originally defined to be a region of overlapped westward and eastward electrojets in the nightside auroral zone [*Heppner*, 1972]. The HD is identified in ground magnetometer data as a reversal in the sign of the north-south component of the geomagnetic field; ionospheric radars typically see a sheared ionospheric flow 1°–2° poleward of the region defined by the magnetic reversal [*Kamide and Vickrey*, 1983; *Koskinen and Pulkkinen*, 1995; *Hughes and Bristow*, 2003]. The HD region has been a focus of significant interest because auroral arcs often break up in its vicinity at the onset of the substorm expansion phase. Some attempts to explain the electrodynamics of the HD have been in terms of dawn-dusk asymmetries in the distribution of plasma across the magnetotail [e.g., *Erickson et al.*, 1991]. The results presented in this paper provide a simple ionospheric explanation for the kinking of streamlines in the outflow region. At high latitudes the convection is strong and predominantly a two-cell pattern driven by the convection electric field; at middle latitudes the nightside convection is much weaker, predominantly westward, and driven by the dynamo action of neutral winds. In the overlap region between these two regimes it is possible for the most equatorward flux tubes of the two-cell convection to become entrained in the weaker westward convection at middle latitudes. In the early morning sector this mixing will produce the kinking of streamlines seen in Figures 11 and 12. One influence that will modulate the degree of mixing between these two regimes is meridional winds produced by auroral heating; another, as explained below, is penetration electric fields under the influence of ionospheric conductance.

[45] So far, we have concentrated the discussion of nightside midlatitude convection on distinguishing between the various sources of electric fields; in particular, magnetospheric sources at high latitudes and neutral dynamo sources at lower latitudes. However, a full consideration of the physics of this region also needs to consider the role of ionospheric conductance. *Senior and Blanc* [1984a] modeled ring current shielding of the midlatitude ionosphere and examined the effect that latitude and local time variations in ionospheric conductivity can have on the ability of magnetospheric electric fields to penetrate into the midlatitude ionosphere. The efficiency of shielding is expected to be lower in the presence of a conducting ionosphere because polarization charges at the edge of the ring current can be easily discharged along equipotential magnetic field lines. *Senior and Blanc* [1984a] found that neglecting this influence of ionospheric conductivity overestimates the efficiency with which magnetospheric electric fields are shielded from penetrating to middle latitudes by a factor of 3. The penetration of magnetospheric electric fields equatorward of the auroral zone in the presence of a realistic conductance distribution produces an asymmetric potential pattern with westward flows across midnight until 0300 MLT [*Senior and Blanc*, 1984b]. This is consistent with Figures 11 and 12. The influence of ionospheric conductivity on reducing the amount of shielding thus provides yet another explanation for the kinking of streamlines in the outflow region shown in Figures 11 and 12.

[46] We conclude this discussion section with some comments about plans to improve the spatial coverage of SuperDARN in the Northern Hemisphere. The analysis in section 3.1.4 provided examples in which additional measurements of high-speed flows obtained by Wallops at

middle latitudes did not always produce a corresponding boost in the cross-polar potential, as might be expected (e.g., Figure 9). This behavior can be attributed to the fact that the potential fitting algorithm can sometimes alter the morphology of existing contours in regions of poor data coverage rather than add new contours to the pattern. The only way to overcome this problem is to increase the coverage of SuperDARN measurements. The recent construction of a SuperDARN radar at Rankin Inlet, Canada, and the proposed addition of a second radar at Inuvik, Canada (the so-called PolarDARN pair), should greatly improve the specification of convection at the highest latitudes of the polar cap. In section 3.1.5 a long-lived SAPS channel was identified in the DMSP drift meter data that was not seen by SuperDARN because of insufficient local time coverage at middle latitudes. Improving the capability for reliable monitoring of SAPS and storm-related convection would require the construction of an entirely new midlatitude array of SuperDARN radars. The results from the Wallops radar presented in this paper have provided the necessary proof of concept for seriously considering such a venture. Indeed, at the present time, a second midlatitude SuperDARN radar is under construction in Hokkaido, Japan. What might a comprehensive array of midlatitude SuperDARN radars look like? In the North American sector, three pairs of collocated radars would be sufficient to provide more than 8 hours of local time coverage at middle latitudes: one pair on the west coast (e.g., Oregon), one pair in the plains (e.g., Kansas), and a second radar at Wallops Island with a northwest look direction. The spatial coverage provided by these six radars would include substantial bistatic measurements at middle latitudes and also overlap with the fields of view of the radars in the higher-latitude array. It would then be possible to test the extent to which the statistical patterns of ionospheric convection displayed in Figures 11 and 12 are true representations of how the midlatitude convection behaves at particular instants in time.

5. Summary and Conclusions

[47] The primary purpose of this paper has been to present the first comprehensive analysis of Doppler velocity measurements from the Wallops radar, which began operations in May 2005. Measurements from the Wallops radar have been examined during the first few hours of a geomagnetic storm that occurred on 31 August 2005, and compared with simultaneous measurements from the other SuperDARN radars, particularly Goose Bay. This event study has demonstrated the unique capabilities of the Wallops radar for monitoring convection during periods of increased geomagnetic activity when the other SuperDARN radars typically suffer a significant reduction in the rate of data capture. SuperDARN now has the ability to view the onset of geomagnetic disturbance in the auroral zone at high latitudes and monitor its subsequent propagation to middle latitudes. The impact of including Wallops data in the calculation of hemispheric convection patterns during the 31 August 2005 event has been examined by comparing convection patterns calculated with and without Wallops data. The F13 and F15 DMSP spacecraft identified a SAPS channel in the postdusk sector that was outside the Wallops field of view. Average convection patterns have been calculated for the period June 2005 to April 2006 and binned by the *Kp* geomagnetic index. During periods of weak-moderate geomagnetic activity, Wallops typically observes a steady westward drift of ionospheric irregularities across much of the nightside, consistent with measurements obtained from the DE 2 spacecraft and the Millstone Hill incoherent scatter radar; however, the magnitude of these drifts during quiet times is larger than what has been measured previously, in part because of inadequate ground-scatter determination. When the midlatitude drifts from Wallops are incorporated into the calculation of SuperDARN convection patterns, the kinking of streamlines in the nightside outflow region becomes accentuated. During periods of increased geomagnetic disturbance the measurements from Wallops capture more of the equatorward extent of the convection and increase the size the average cross-polar potential by 25%. In conclusion, measurements from the Wallops radar are providing important new measurements of the large-scale pattern of ionospheric convection at middle latitudes that have not been previously available from SuperDARN.

[48] **Acknowledgments.** Construction of the Wallops radar was made possible by funds provided by the Johns Hopkins University Applied Physics Laboratory and the NASA Wallops Flight Facility. Financial support for the research presented conducted at JHU/APL has been provided by NSF grant ATM-0418101 and NASA grant NNG04GA12G; Marc Hairston acknowledges support from NSF grant ATM-0228207. Operation of the Northern Hemisphere SuperDARN radars is supported by the national funding agencies of Canada, France, Japan, the United Kingdom, and the United States. The *SYM-H* index was obtained from the World Data Center at Kyoto. The *Kp* index was obtained from the CEDAR database. We thank the ACE MAG and SWEPAM instrument teams and the ACE Science Center for providing interplanetary data.

[49] The Editor thanks John Foster and Stephen Milan for their assistance in evaluating this paper.

References

Anderson, P. C., et al. (1991), The ionospheric signatures of rapid subauroral drifts, *J. Geophys. Res.*, *96*, 5785.

Anderson, P. C., D. L. Carpenter, K. Tsuruda, T. Mukai, and F. J. Rich (2001), Multisatellite observations of rapid subauroral ion drifts (SAID), *J. Geophys. Res.*, *106*, 29,585.

Baker, K. B., and S. Wing (1989), A new magnetic coordinate system for conjugate studies at high latitude, *J. Geophys. Res.*, *94*, 9139.

Basu, S. (2001), Ionospheric effects of major magnetic storms during the International Space Weather Period of September and October 1999: GPS observations, VHF/UHF scintillations, and in situ density structures at middle and equatorial latitudes, *J. Geophs. Res.*, *106*, 30,389.

Blanc, M., and P. Amayenc (1979), Seasonal variation of the ionospheric $\mathbf{E} \times \mathbf{B}$ drifts, *J. Geophys. Res.*, *84*, 2691.

Blanc, M., and A. D. Richmond (1980), The ionospheric disturbance dynamo, *J. Geophys. Res.*, *85*, 1669.

Blanc, M., P. Amayenc, P. Bauer, and C. Taieb (1977), Electric field induced drifts from the French incoherent scatter facility, *J. Geophys. Res.*, *82*, 87.

Buonsanto, M. J., and O. G. Witasse (1999), An updated climatology of thermospheric neutral winds and F region ion drifts above Millstone Hill, *J. Geophys. Res.*, *104*, 24,675.

Buonsanto, M. J., M. E. Hagan, J. E. Salah, and B. G. Fejer (1993), Solar cycle and seasonal variations in F region electrodynamics at Millstone Hill, *J. Geophys. Res.*, *98*, 15,677.

Burke, W. J., N. C. Maynard, M. P. Hagan, R. A. Wolf, G. R. Wilson, L. C. Gentile, M. S. Gussenhoven, C. Y. Huang, T. W. Garner, and F. J. Rich (1998), Electrodynamics of the inner magnetosphere observed in the dusk sector by CRESS and DMSP during the magnetic storm of June 4–6, 1991, *J. Geophys. Res.*, *103*, 29,399.

Chisham, G., M. P. Freeman, I. J. Coleman, M. Pinnock, M. R. Hairston, M. Lester, and G. Sofko (2004), Measuring the dayside reconnection rate during an interval of due northward interplanetary magnetic field, *Ann. Geophys.*, *22*, 4243.

Christensen, A. B., et al. (2003), Initial observations with the Global Ultraviolet Imager (GUVI) in the NASA TIMED satellite mission, *J. Geophys. Res.*, *108*(A12), 1451, doi:10.1029/2003JA009918.

Crooker, N. U. (1979), Dayside merging and cusp geometry, *J. Geophys. Res.*, *84*, 951.

Dungey, J. W. (1961), Interplanetary magnetic field and the auroral zones, *Phys. Rev. Lett.*, *93*, 47.

Erickson, G. M., R. W. Spiro, and R. A. Wolf (1991), The physics of the Harang discontinuity, *J. Geophys. Res.*, *96*, 1633.

Fejer, B. G., and M. C. Kelley (1980), Ionospheric irregularities, *Rev. Geophys.*, *18*, 401.

Foster, J. C. (1987), Radar-deduced models of the convection electric field, in *Quantitative Modeling of Magnetosphere-Ionosphere Coupling Processes*, edited by Y. Kamide, pp. 71–76, Kyoto Sangyo Univ., Kyoto, Japan.

Foster, J. C., and W. J. Burke (2002), A new characterization for subauroral electric fields, *Eos AGU Trans.*, *83*, 393.

Foster, J. C., and F. J. Rich (1998), Prompt midlatitude electric field effects during severe geomagnetic storms, *J. Geophys. Res.*, *103*, 26,367.

Foster, J. C., and H. B. Vo (2002), Average characteristics and activity dependence of the subauroral polarization stream, *J. Geophys. Res.*, *107*(A12), 1475, doi:10.1029/2002JA009409.

Friis-Christensen, E., Y. Kamide, A. D. Richmond, and S. Matsushita (1985), Interplanetary magnetic field control of high-latitude electric fields and currents determined from Greenland magnetometer data, *J. Geophys. Res.*, *90*, 1325.

Galperin, Y. I., et al. (1974), Plasma convection in the polar ionosphere, *Ann. Geophys.*, *30*, 1.

Greenwald, R. A., K. B. Baker, R. A. Hutchins, and C. Hanuise (1985), An HF phased-array radar for studying small-scale structure in the high-latitude ionosphere, *Radio Sci.*, *20*, 63.

Greenwald, R. A., et al. (1995), DARN/SuperDARN: A global view of high-latitude convection, *Space Sci. Rev.*, *71*, 763.

Greenwald, R. A., K. Oksavik, P. J. Erickson, F. D. Lind, J. M. Ruohoniemi, J. Baker, and J. W. Gjerloev (2006), Identification of the temperature gradient instability as the source of decameter scale ionosphere irregularities on plasmapause field lines, *Geophys. Res. Lett.*, *33*, L18105, doi:10.1029/2006GL026581.

Heelis, R. A., W. B. Hanson, C. R. Lippincott, D. R. Zuccaro, L. H. Harmon, B. J. Holt, J. E. Doherty, and R. A. Power (1981), The ion drift meter for Dynamics Explorer-B, *Space Sci. Instrum.*, *5*, 511.

Heelis, R. A., and W. R. Coley (1992), East-west ion drifts at mid-latitudes observed by Dynamics Explorer 2, *J. Geophys. Res.*, *97*, 19,461.

Heppner, J. P. (1972), The Harang discontinuity in auroral belt ionospheric currents, *Geofys. Publ.*, *29*, 105.

Heppner, J. P. (1977), Empirical models of high-latitude electric fields, *J. Geophys. Res.*, *82*, 1115.

Heppner, J. P., and N. C. Maynard (1987), Empirical high-latitude electric field models, *J. Geophys. Res.*, *92*, 4467.

Holt, J. M., R. H. Wand, J. V. Evans, and W. L. Oliver (1987), Empirical models for the plasma convection at high latitudes from Millstone Hill observations, *J. Geophys. Res.*, *92*, 203.

Holzworth, R. H., and C.-I. Meng (1975), Mathematical representation of the auroral oval, *Geophys. Res. Lett.*, *2*, 377.

Huang, C.-S., J. C. Foster, and J. M. Holt (2001), Westward plasma drift in the midlatitude ionospheric *F* region in the midnight-dawn sector, *J. Geophys. Res.*, *106*, 30,349.

Huang, C., S. Sazykin, R. Spiro, J. Goldstein, G. Crowley, and J. M. Ruohoniemi (2006), Storm-time penetration electric fields and their effects, *Eos Trans. AGU*, *87*(13), 131.

Hughes, J. M., and W. A. Bristow (2003), SuperDARN observations of the Harang discontinuity during steady magnetospheric convection, *J. Geophys. Res.*, *108*(A5), 1185, doi:10.1029/2002JA009681.

Kamide, Y., and J. F. Vickrey (1983), Variability of the Harang discontinuity as observed by the Chatanika radar and the IMS Alaska magnetometer chain, *Geophys. Res. Lett.*, *10*, 159.

Koskinen, H. E. J., and T. I. Pulkkinen (1995), Midnight velocity shear zone and the concept of Harang discontinuity, *J. Geophys. Res.*, *100*, 9539.

McComas, D. J., S. J. Blame, P. Barker, W. C. Feldman, J. L. Phillips, P. Riley, and J. W. Griffee (1998), Solar Wind Electron Proton Alpha Monitor (SWEPAM) for the Advanced Composition Explorer, *Space Sci. Rev.*, *86*, 563.

Milan, S. E., M. Lester, S. W. H. Cowley, and M. Brittnacher (2000), Dayside convection and auroral morphology during an interval of northward planetary magnetic field, *Ann. Geophys.*, *18*, 436.

Nishitani, N., T. Ogawa, N. Sato, H. Yamagishi, M. Pinnock, J.-P. Villain, G. Sofko, and O. Troshichev (2002), A study of the dusk convection cell's response to an IMF southward turning, *J. Geophys. Res.*, *107*(A3), 1036, doi:10.1029/2001JA900095.

Oksavik, K., R. A. Greenwald, J. M. Ruohoniemi, M. R. Hairston, L. J. Paxton, J. B. H. Baker, J. W. Gjerloev, and R. J. Barnes (2006), First observations of the temporal/spatial variation of the subauroral polarization stream from the SuperDARN Wallops Island HF radar, *Geophys. Res. Lett.*, *33*, L12104, doi:10.1029/2006GL026256.

Papitashvili, V. O., B. A. Belov, D. S. Faermark, Y. I. Feldstein, S. A. Golyshev, L. I. Gromova, and A. E. Levitin (1994), Electric potential patterns in the northern and southern polar regions parameterized by the interplanetary magnetic field, *J. Geophys. Res.*, *99*, 13,251.

Reiff, P. H., and J. L. Burch (1985), IMF B_y-dependent plasma flow and Birkeland currents in the dayside magnetosphere: 2. A global model for northward and southward IMF, *J. Geophys. Res.*, *90*, 1595.

Rich, F. J., and M. Hairston (1994), Large-scale convection patterns observed by DMSP, *J. Geophys. Res.*, *99*, 3827.

Ruohoniemi, J. M., and K. B. Baker (1998), Large-scale imaging of high-latitude convection with Super Dual Auroral Radar Network HF radar observations, *J. Geophys. Res.*, *103*, 20,797.

Ruohoniemi, J. M., and R. A. Greenwald (1996), Statistical patterns of high-latitude convection obtained from Goose Bay HF radar observations, *J. Geophys. Res.*, *101*, 21,743.

Ruohoniemi, J. M., and R. A. Greenwald (1998), The response of high-latitude convection to a sudden southward IMF turning, *Geophys. Res. Lett.*, *25*, 2913.

Ruohoniemi, J. M., and R. A. Greenwald (2005), Dependencies of high-latitude plasma convection: Consideration of interplanetary magnetic field, seasonal, and universal time factors in statistical patterns, *J. Geophys. Res.*, *110*, A09204, doi:10.1029/2004JA010815.

Ruohoniemi, J. M., R. A. Greenwald, K. B. Baker, J.-P. Villain, and M. A. McCready (1987), Drift motions of small-scale irregularities in the high-latitude *F* region: An experimental comparison with plasma drift motions, *J. Geophys. Res.*, *92*, 4553.

Senior, C., and M. Blanc (1984a), On the control of magnetospheric convection by the spatial distribution of ionospheric conductivities, *J. Geophys. Res.*, *89*, 261.

Senior, C., and M. Blanc (1984b), Convection in the inner magnetosphere: Model predictions and data, *Ann. Geophys.*, *5*, 405.

Shepherd, S. G., and J. M. Ruohoniemi (2000), Electrostatic potential patterns in the high-latitude ionosphere constrained by SuperDARN measurements, *J. Geophys. Res.*, *105*, 23,005.

Smith, C. W., M. H. Acuna, L. F. Burlaga, J. L. Heureux, N. F. Ness, and J. Schiefele (1998), The ACE magnetic field experiment, *Space Sci. Rev.*, *86*, 613.

Spiro, R. W., R. A. Heelis, and W. B. Hanson (1978), Rapid subauroral ion drifts observed by Atmosphere Explorer C, *Geophys. Res. Lett.*, *6*, 657.

Villain, J. P., R. A. Greenwald, and J. F. Vickrey (1984), HF ray tracing at high latitudes using measured meridional electron density distributions, *Radio Sci.*, *19*, 359.

Wand, R. H., and J. V. Evans (1981), Seasonal and magnetic activity variations of ionospheric electric fields over Millstone Hill, *J. Geophys. Res.*, *86*, 103.

Watanabe, M., G. J. Sofko, D. A. Andre, T. Tanaka, and M. R. Hairston (2004), Polar cap bifurcation during steady state northward interplanetary magnetic field with $|BY| \sim BZ$, *J. Geophys. Res.*, *109*, A01215, doi:10.1029/2003JA009944.

Weimer, D. R. (1995), Models of high-latitude electric potentials derived with a least error fit of spherical harmonic coefficients, *J. Geophys. Res.*, *100*, 19,595.

Yeh, H.-C., J. C. Foster, F. J. Rich, and W. Swider (1991), Storm time electric field penetration observed at midlatitude, *J. Geophys. Res.*, *96*, 5707.

J. B. H. Baker, J. W. Gjerloev, R. A. Greenwald, K. Oksavik, L. J. Paxton, and J. M. Ruohoniemi, Applied Physics Laboratory, Johns Hopkins University, 11100 Johns Hopkins Road, Laurel, MD 20723-6099, USA. (joseph.baker@jhuapl.edu)

M. R. Hairston, William B. Hanson Center for Space Sciences, University of Texas at Dallas, P.O. Box 830688 FO22, Richardson, TX 75083-0688, USA.